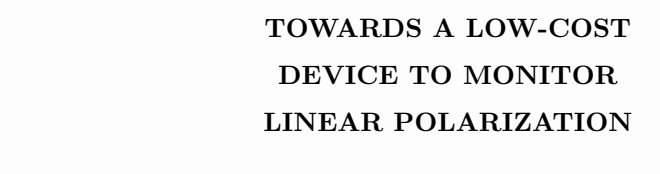
# CRAFTING A CONICAL REFRACTION POLARIMETER

- REDUCED VERSION -



BY Xabier Oianguren Asua

THESIS SUPERVISOR
Alex Turpin Avilés



Bachelor's Thesis Computational Mathematics and Data Analytics 2021-2022

# Crafting a Conical Refraction Polarimeter - REDUCED VERSION -

by Xabier Oianguren Asua

# Contents

Introduction	1
Part A: The Essence of the Polarimeter	2
1. Derivation of Conical Refraction from Maxwell's Equations	2
2. The Belsky-Khapalyuk-Berry Description of the Phenomenon	4
3. Simulating the Phenomenon	6
4. A Natural Polarimeter	9
Part B: The Mind of the Polarimeter	11
1. The Computer Vision Task and the General Quandary	12
2. Artificial Noise	12
3. The Simulated Image Datasets	13
4. Preprocessing	14
5. Optimization Algorithms	16
6. The Geometric Algorithms	16
7. Basic Black-Box Algorithms	27
8. Embedding Space Algorithms	27
9. Simulation Fitting Algorithms	31
10. Pipeline to Compare The Algorithms and Preprocessings	32
Part C: The Body of the Polarimeter	35
1. Experimental Setup to Observe Conical Refraction Rings	35
2. Non-Idealities in the Experimental Rings	37
3. The Experimental Image Dataset	38
4. The Polarimeter, a Proof of Concept	39
Conclusions and Future Work	44
References	15

# Introduction

# Abstract

If one lights a biaxial crystal along its optical axis, the light beam opens in a conical shape and gets out as a hollow ring. This is known as Conical Refraction (CR). At each point along the ring, the light is linearly polarized, with an angle that rotates continuously as one moves along the ring. This happens irrespective of the input light's polarization state. Then, if the input was already linearly polarized, the ring component of its orthogonal polarization will have no light. The intensity continuously increases from there until the angular spot corresponding to the polarization angle of the input beam. This generates a crescent-moon-like shape, which encodes the linear polarization state of the input beam in the degree of rotation of the crescent moon relative to the crystal. This phenomenon was employed in [14, 15] to build a full Stokes polarimeter and in [13] for an (incomplete) polarimeter to measure changes in linear polarization. To do this a computer vision step is essential in order to convert the crescent rings into angle measurements. The computational solutions for this, offered in Refs. [13, 14, 15] were functional, but did not explore all the algorithmic landscape. In this work we will deeply explore the possible algorithms analyzing the theoretical symmetries and the experimental problems they face, in order to distill the best possible solution. With it, following the suggested hardware in Ref. [13], after a small study, we build a functional proof-of-concept polarimeter with an integrated graphical user interface to measure variations of linear polarization in real time. We finally analyze its commercial viability.

# Guideline

The present dissertation is divided into three parts. In part A we study the theoretical framework that allows the prediction of CR, both to have a deep understanding of the symmetries of the crescent rings that can be exploited in the algorithms, and to understand which ones are the experimental requirements of the device. Very importantly, this will provide us the means to simulate the phenomenon. Part A is the part that will be most interesting for the mathematician reader. (This part is heavily trimmed in the summarized version for it is a pedagogical revision of the essential theory).

In part B, the core and main merit of the work, the previously unexplored algorithmic landscape is exhaustively walked through, by offering detailed solutions of very different nature, together with tips for their implementation. These are benchmarked in a big final test over the several datasets generated for the work. (This one will be the most interesting part for the computer-science reader.)

Finally, in Part C, we briefly review the experimental CR phenomenon and infer the practical blocks that should compose a polarimeter based on this phenomenon. With them, a proof-of-concept device is created, tested and compared with the current market options, looking for potential niches in which it could be industrially specialized. (This is the part that the engineer will enjoy the most).

# Disclaimer on the Length of the Work

Because the thesis could have an arbitrary number of pages, all the concepts and remarks required for completeness and to leave a self-contained dissertation were included. However, a summarized version was composed (which is the present document) dedicated for the thesis qualifying board, which has multiple additional works to correct. The full dissertation, together with all the generated computational material and results can be found in the project Github, Ref. [23].

# Part A: The Essence of the Polarimeter

In this first section, we will review the basic theoretical framework predicting the Conical Refraction (CR) phenomenon on which the developed polarimeter will be based. We will first derive the existence of the phenomenon from Maxwell's equations, by introducing all the notation and physics jargon that we will be employing throughout the work. We will then review the most complete description of the phenomenon so far, which will allow us to simulate it and generate theoretical predictions of what we will see in the laboratory. After noting the main features of a conically refracted beam, the idea underlying the intended polarimeter will emerge naturally.

# A.1. Derivation of Conical Refraction from Maxwell's Equations

This section can be found in the full version of the dissertation [1]. It is an introduction to crystal optics that allows the prediction of the CR phenomenon in a beautiful way, by only assuming the reader is familiar with Maxwell's equations. To write it, several text books were consulted, among them references [2, 3, 4].

In this reduced version, we only leave the description of what polarization is, together with an introductory approach to CR.

# The Polarization of Light

A transverse wave is a traveling wave that oscillates in a perpendicular direction to the wavefront propagation direction. The **polarization** is then given by the pattern shaped by the transversally oscillating component of the wave. Since in the case of electromagnetic waves like the sinusoidal plane waves described in the full text, the electric and magnetic field vectors (or the displacement and magnetization fields for anisotropic media) are always mutually orthogonal and orthogonal to the propagation direction, they are transverse waves and we can define a polarization state for them. In fact, their magnitudes are uniquely related by a constant, so studying, say, the electric field's polarization will suffice.

For plane waves, it is proved in the full text that the electric field vector will only have the freedom to oscillate in the orthogonal plane to the propagation direction. Thus, let us choose the z axis as the propagation direction, such that the electric field  $\vec{E}(\vec{r},t) = E_x(\vec{r},t)\hat{x} + E_y(\vec{r},t)\hat{y} + E_z(\vec{r},t)\hat{z}$  will have  $E_z \equiv 0$ , where  $\hat{x}, \hat{y}, \hat{z}$  are the unit vectors of our Cartesian frame of reference and  $\vec{r} := (x, y, z) \in \mathbb{R}^3$  is the position vector in this basis.  $t \in \mathbb{R}$  denotes the time of observation. Now, consider the sinusoid of spatial and temporal frequencies  $\vec{k} \in \mathbb{R}^3$  and  $w \in \mathbb{R}$ :

$$\vec{E}(\vec{r},t) = E_{0x} \cos(\vec{k} \cdot \vec{r} - wt + \phi_x)\hat{x} + E_{0y} \cos(\vec{k} \cdot \vec{r} - wt + \phi_y)\hat{y}$$
(1)

with  $E_{0x}, E_{0y}, \phi_x, \phi_y \in \mathbb{R}$  real degrees of freedom. The x component of the net vector  $\vec{E}$  is a cosine oscillating up and down in  $\hat{x}$ , while the y component oscillates left-right in  $\hat{y}$  at the same frequency in time and space as x, but possibly unsynchronized. This synchronization will be given by "how advanced" the cosine's oscillations are relative to each other. We call this relative argument distance, the **relative phase**  $\Delta \phi := \phi_x - \phi_y$ . Allowing  $\Delta \phi$  to be any number we allow for a fixed  $\vec{r}, t$ , the net vector  $\vec{E}$  to point in any of the directions in the xy plane. However, we realize that the traced shape by the vector  $\vec{E}$  while t or  $\vec{r}$  advance, also depends on the **relative magnitudes**  $E_{0x}/E_{0y}$  of the components. For example, we know by only saying the relative phase is  $\pi/2$  (such that the cosines are a quarter of period de-phased, coinciding the zero of one cosine with the maximum amplitude of the other), that the net electric vector will rotate in the xy plane. However, it will trace a perfect circle if  $E_{0x} = E_{0y}$ , while it will trace an ellipse otherwise (assuming  $E_{0x}, E_{0y}$  are non-zero). This ellipse

will have its major axes oriented and scaled as a function of  $E_{0x}/E_{0y}$ . These two traced patterns or polarizations of a plane wave are called **circular** and **elliptical polarizations** (CP and EP) respectively, which can further be specified to be left- or right-handed, as a function of the direction of rotation. In fact, there is only one additional polarization state left. If either of  $E_{0x}$ ,  $E_{0y}$  are zero, then the net vector will only oscillate in x or y. If the relative phase is of any multiple of  $\pi$  (the maximum amplitudes of the cosines coincide), then the net vector will also oscillate in a fixed plane. This is called **linear polarization**. It is determined by the angle relative to the x axis at which the vector oscillates. Since there are no more patterns a sinusoidal wave can take, we conclude that the state of polarization is uniquely determined by the relative phase and the relative magnitudes of the field components. In reality, light can also be unpolarized if it is a mixture of differently polarized plane waves, or randomly polarized if this mixture is stochastic, but we will not consider them in this work, since the input light will be something under our control.

Lastly, we can gather in a single terms all the polarization information. We had that:  $E_j(\vec{r},t) = E_{0j}cos(\vec{k}\cdot\vec{r}-wt+\phi_j) = \Re e\Big\{E_{0j}^{i\phi_j}e^{i(\vec{k}\cdot\vec{r}-wt)}\Big\}$  for all  $j\in x,y$ . We can factor out the exponential and the magnitude of the vector  $E_0^2:=E_{0x}^2+E_{0y}^2$  to have:

$$\vec{E}(\vec{r},t) = \Re \left\{ \hat{u}_J E_0 e^{i(\vec{k}\cdot\vec{r}-wt)} \right\}$$
 (2)

Where  $\hat{u}_J = \frac{1}{E_0} (E_{0x} e^{i\phi_x} \hat{x} + E_{0y} e^{i\phi_y} \hat{y})$  is a unit vector in  $\mathbb{C}^2$  giving all the information about the polarization of the wave (the relative magnitude and phase). Because in general we do not care about the common cumulative phase of both components to know the polarization, we identify  $\hat{u}_J$  with  $e^{i\varphi}\hat{u}_J$   $\forall \varphi \in \mathbb{R}$ . This "neglected" multiplicative factor is called a **global phase**. The unit vector  $\hat{u}_J$  is called the **Jones vector** or polarization vector.

Note that working with complex plane waves is very useful also because now, adding a relative phase shift between the components of polarization is just about multiplying a unit complex number to one component of the Jones vector. This means that if we allow linear operations on the electric field to be over complex coefficients (taking the real part after the operation), we will be able to easily play with the relative phases and the polarization as well. For all this practicality, in the remaining we will assume the real part operation for electric field plane waves and **we will omit the explicit**  $\Re\{\cdot\}$  operation.

#### Qualitative Description of Conical Refraction

As proved in detail in the full dissertation, if a light beam enters a biaxial crystal with its main wave-vector (in the Fourier decomposition) aligned with one of the two optical axes of the crystal, it will refract not as a single beam (as in typical refraction), nor as two beams (as in birefringence), but as a conical bouquet of "infinite" rays. Therefore, inside the crystal the light beam will open into a hollow cone of light. Once the cone of light arrives to the end face of the crystal, it will get out as a hollow ring of light. This is what Hamilton called **Conical Refraction (CR)**. See a schematic picture in Figure 1.

The characteristics of the conically refracted beam and the generated rings are qualitatively (and quite quantitatively as we will see) determined by three parameters. The first one is the **semi-angle** of the cone  $\alpha$ , which can be geometrically proven using Fresnel's surface to be  $\alpha = \sqrt{(\varepsilon_y - \varepsilon_x)(\varepsilon_z - \varepsilon_y)/\varepsilon_y}$  for  $\varepsilon_x < \varepsilon_y < \varepsilon_z$ , the eigenstates of the electric permittivity matrix. Then, given the length of the biaxial crystal slab L along the optical axis, we can get the **geometric radius** of the hollow ring to be  $R_0 = L \tan(\alpha)$ . It can be proven geometrically that the cone is slanted such that it opens in the plane of the two optical axes, as shown in Figure 1. Finally, since in our experiments, the input

<sup>&</sup>lt;sup>1</sup>It is interesting to note that this polarization state space is then equal to the space of representation of a two dimensional quantum system (a qubit). This, together with the fact that the most relevant classical optical devices are linear (they act as linear operators on the electric field), justify why light polarization is also employed as a "qubit" for quantum experiments.

beam will have a Gaussian profile in the transversal section to the propagation, we need to define its width, which we call the **beam waist**  $w_0$ . This parameter will determine how many plane wave components around the conical singularity of the Fresnel surface compose the input beam. Thus, it will be proportional to the width of the generated hollow ring. The numerical definition of the beam waist  $w_0$  is the full width at half maximum (divided by  $\sqrt{2log(2)}$ ) for the transverse intensity of the light beam at the focal plane, where the Gaussian profile gets most concentrated.

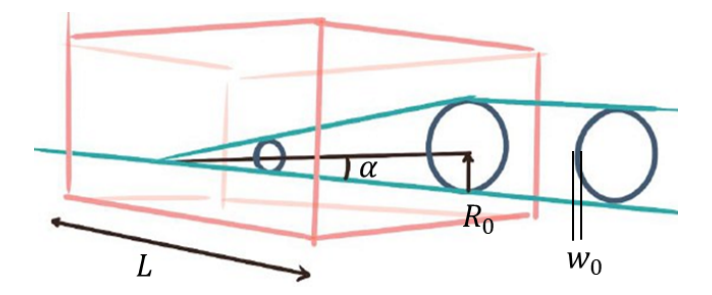


Figure 1: Schematic depiction of the classical description of conical refraction, with its main parameters.

Before we continue, it is important to note that it turns out the most defined picture of the ring is generated only at infinity (far away from the entry point), which is the reason why a focusing lens will be used before the beam enters to the crystal: it will take the image formed at infinity to the focal plane, which is at a finite distance. Finally, note that the generated rings, as explained in detail in the full text, are split in two rings by a dark circumference called the **Poggendorff ring** (where the ideal cone of Hamilton should be placed, and which defines  $R_0$ ).

# A.2. The Belskii-Khapalyuk-Berry Description of the Phenomenon

So far we have understood when the phenomenon happens and which is the shape of the overal light beam. Yet, we have not seen what happens with the state of polarization, which will be the key to develop the polarimeter. To understand this and to be able to simulate the phenomenon, we will need to introduce part of the full diffractive theory in biaxial crystals developed by Belskii and Khapalyuk in 1978 [5, 6], which was reformulated (and extended) by Michael Berry in 2004 [7]. We will proceed to present the cylindrically symmetric solution, as presented by Alex Turpin in Ref. [10].

Let us consider a biaxial crystal with mean refractive index n and one of its optical axes aligned with the z Cartesian coordinate axis. Before the crystal a focusing lens will be placed as explained above, so we will consider the z coordinate is centered in the focal plane. In addition, we will consider the coordinates x, y are in waist radius  $w_0$  units, while z is in Rayleigh length units  $z_R := \pi w_0^2 n/\lambda$ , being  $\lambda$  the main wavelength of the input beam. Finally, we will consider an input light beam  $\vec{D}_0(\vec{r})$  with its spatial Fourier decomposition in plane waves, such that all the expansion weights are centered around one  $\vec{k}$  with a particular  $k_z$  directed in the z axis,  $k_z > 0$ . We will assume that for all significant  $\vec{k}$  in its decomposition,  $k_z >> k_x, k_y$ . This is called the paraxial approximation. It implies, as we saw, not only that the displacement field will have null component in z, but also that the other two components will vary sinusoidally in the z direction, allowing us to center our attention in the distribution of the electric field only in the transversal plane z = 0,  $\vec{D}(\vec{q};z) = (D_x(\vec{q};z), D_y(\vec{q};z), 0)$  with  $\vec{q} := (x,y)$ . In addition we will assume that after passing through a medium, the light beam is describable with its displacement vector  $\vec{D}$  (for the effect of bound charges will become negligible).

The approach followed in the Belskii-Kahapalyuk-Berry (BKB) formulation is to first derive the effect that the biaxial crystal has on a particular plane wave with transversal wavenumber  $\vec{k} = (k_x, k_y)$  (the dominant  $k_z$  component is presumed). Then if we decompose the input wave in its transversal Fourier spectrum and apply the effect to each plane wave component, by the linearity of Maxwell's equations, we will get the evolution of the entire wave. Remember that what gave the CR ring its pattern were actually the plane wave components that were close but not equal to the singularity

 $\vec{k}$  exactly aligned with the optical axis, for which  $k_x, k_y = 0$ . This fact is here made explicit when considering the distribution of all the rest of components.

Berry proves in [7, 8] that a lowly birefringent biaxial crystal causes a unitary transformation  $U(\vec{k}) = e^{-i\Gamma(\vec{k})}$  to an input plane wave  $\vec{k}$  close to the singularity, such that  $\Gamma$  is the Hermitian operator  $\Gamma(\vec{k}) := \frac{1}{2}|\vec{k}|^2z^2Id + \rho_0\vec{k}\cdot(\sigma_z,\sigma_x)$ . Here,  $\sigma_z,\sigma_x$  denote the x and z Pauli matrices and we define  $\rho_0 \equiv R_0/w_0$  to be the geometric radius of the CR ring in waist radius units (or the ratio between the geometric radius of the ring and the waist radius of the beam). Then, by considering the identity  $e^{i\vec{v}(\vec{n}\cdot\vec{\sigma})} = Id\cos(v) + i(\vec{n}\cdot\vec{\sigma})\sin(v)$  given a vector  $\vec{v} = v\vec{n}$  with  $|\vec{n}| = 1$  and given  $\vec{\sigma} = (\sigma_x, \sigma_y, \sigma_z)$  is the vector of Pauli matrices, we can rewrite the unitary as:

$$\boldsymbol{U}(\vec{k}) = e^{-i\frac{1}{2n}|\vec{k}|^2 z^2} \left[ cos\left(\rho_0|\vec{k}|\right) \boldsymbol{I}\boldsymbol{d} + i \, sin\left(\rho_0|\vec{k}|\right) \frac{\vec{k}}{|\vec{k}|} \cdot (\boldsymbol{\sigma_z}, \boldsymbol{\sigma_x}) \right]$$
(3)

Given the transversal Fourier transform of the input beam  $\vec{D}_0(\vec{q}) = (D_{0x}(\vec{q}), D_{0y}(\vec{q}))$  in  $\vec{k} = (k_x, k_y)$ :

$$A_x(\vec{k}) := \frac{1}{(2\pi)^2} \iint_{\mathbb{R}^2} D_{0x}(\vec{q}) e^{-i\vec{k}\cdot\vec{r}} dx \ dy \qquad A_y(\vec{k}) := \frac{1}{(2\pi)^2} \iint_{\mathbb{R}^2} D_{0y}(\vec{q}) e^{-i\vec{k}\cdot\vec{r}} dx \ dy \qquad (4)$$

We can obtain the post-crystal displacement vector field (remember it has only component in x, y) by applying the unitary transformation to the plane wave coefficients of the input beam  $\vec{A}(\vec{k})$  and then taking the result back to position space:

$$\vec{D}(\vec{q};z) = \frac{1}{(2\pi)^2} \iint_{\mathbb{R}^2} e^{i\vec{k}\cdot\vec{q}} \mathbf{U}(\vec{k}) \vec{A}(\vec{k}) dk_x dk_y$$
 (5)

This can be expanded to a simpler form in cylindrical coordinates  $\vec{k} = k(\cos(\phi_k), \sin(\phi_k))$ ,  $\vec{q} = q(\cos(\varphi), \sin(\varphi))/w_0$  with  $\phi_k, \varphi \in [-\pi, \pi)$  and q, k > 0 as:

$$\vec{D}(q,\varphi;z) = \frac{1}{(2\pi)^2} \int_{-\pi}^{\pi} \int_{0}^{\infty} e^{ikq\cos(\phi_k - \varphi)} e^{-i\frac{1}{2n}k^2z^2} \begin{pmatrix} \cos(\phi_k) & \sin(\phi_k) \\ \sin(\phi_k) & -\cos(\phi_k) \end{pmatrix} \vec{A}(\vec{k}) \ k \ dk \ d\phi_k \qquad (6)$$

We now consider that the input beam is cylindrically symmetric with a uniform polarization  $\vec{E}(\vec{q}) = E(q)\hat{u}_J$ , with  $\hat{u}_J$  its Jones vector. Its Fourier transform will also be cylindrically symmetric, such that  $A_x(\vec{k}) = A_y(\vec{k}) = a(k) := \int_0^\infty E(q)J_0(qk)kdr$ , where  $J_n(x)$  is the  $n^{th}$  order Bessel function of the first type. This assumption then allows integrating equation (6) over  $\phi_k$ , using the Bessel function identities:  $\int_{-\pi}^{\pi} e^{ik\rho\cos(\phi_k-\varphi)}d\phi_k = J_0(k\rho)$  and  $\int_{-\pi}^{\pi} e^{ik\rho\cos(\phi_k-\varphi)}\cos(\phi_k)d\phi_k = \cos(\varphi)J_1(k\rho)$ . This leaves the computation of  $\vec{D}$  as a one dimensional integral:

$$\vec{D}(q,\varphi;z) = \begin{pmatrix} B_0(q;z) + B_1(q;z)\cos\varphi & B_1(q;z)\sin\varphi \\ B_1(q;z)\sin\varphi & B_0(q;z) - B_1(q;z)\cos\varphi \end{pmatrix} \hat{u}_J$$
 (7)

where  $B_0, B_1$  are known as the BKB integrals, which note that only depend on q, z:

$$B_0(q;z) = \frac{1}{2\pi} \int_0^\infty a(k)e^{-i\frac{k^2z^2}{2n}}\cos(k\rho_0)J_0(kq)k \ dk \tag{8}$$

$$B_1(q;z) = \frac{1}{2\pi} \int_0^\infty a(k)e^{-i\frac{k^2z^2}{2n}} \sin(k\rho_0) J_1(kq)k \ dk \tag{9}$$

Finally, we can get the intensity pattern of light  $I(q, \varphi; z)$ , by taking the magnitude squared of  $\vec{D}$  (its real part). This intensity pattern in  $q, \varphi$  for a fixed z is what we expect to be captured by a camera (or our eye) if the sensor is placed orthogonal to the optical axis at a distance z from the focal plane.

#### A.2.1. The angular shape of the emerging pattern depends on the input polarization

We can now predict what we will see/capture as a function of the polarization of the input beam. If we evaluate in equation (7) the Jones vector for circular polarization (CP),  $\vec{u}_J = \frac{1}{\sqrt{2}}(1, \pm i)$  (a quarter period relative phase  $e^{i\pi/2} = i$ ), we can easily arrive at:

$$I_{CP}(q,\varphi;z) = |\Re\{\vec{D}(q,\varphi;z)\}|^2 = |B_0(q;z)|^2 + |B_1(q;z)|^2$$
(10)

Since  $B_0, B_1$  do not depend on  $\varphi$ , we see that the intensity pattern for CP only depends radially on q,  $I_{CP}(q, \varphi; z) = I_{CP}(q; z)$ . This implies that the intensity pattern is symmetric in its angular component. That is, if we take the integral in q for the intensity pattern:

$$\mathcal{I}_{CP}(\varphi;z) = \int_0^\infty I_{CP}(q,\varphi;z)q \, dq = C(z) \tag{11}$$

we get a same value C for all  $\varphi$  (for a fixed z).<sup>2</sup> This is in accordance with out intuition that a hollow ring should be generated.

If instead we evaluate the Jones vector for an arbitrary linear polarization (LP) at an angle  $\Phi_{LP}$  with the x axis, say  $\vec{u}_J = (cos\Phi_{LP}, sin\Phi_{LP})$ , after several trigonometric identities and some hard work, we can arrive to:

$$I_{\Phi_{LP}}(q,\varphi;z) = I_{CP}(q;z) + 2\Re\{B_0(q;z)B_1^*(q;z)\}\cos(2\Phi_{LP} - \varphi)$$
(12)

where  $b^*$  denotes complex conjugation of  $b \in \mathbb{C}$ . We can derive an important result here. Following Berry and Jeffrey [7, 8, 9], since we are interested in thick crystal slabs and light beams with small waist, such that  $R_0 >> w_0$ , around z = 0, we can plug asymptotic expressions for the Bessel functions in  $B_0, B_1$  for we consider large enough q. Up to oscillatory terms that become negligible when integrated, we can then consider:

$$cos(k\rho_0)J_0(kq) \simeq sin(k\rho_0)J_1(kq) \tag{13}$$

This makes  $B_0(q;0) \simeq B_1(q;0)$  for the significant values on the ring, yielding for the linear polarization intensity (12), (by using  $1 + \cos(x) = 2\cos^2(x/2)$ ):  $I_{\Phi_{LP}}(q,\varphi;z) = 2|B_0(q;0)|^2\cos^2(\varphi/2 - \Phi_{LP})$ . The angular pattern will then be:

$$\mathcal{I}_{\Phi_{LP}}(\varphi;z) = C(z)\cos^2(\frac{\varphi}{2} - \Phi_{LP}) \tag{14}$$

This means that if we input a light beam with a linear polarization at an angle  $\Phi_{LP}$  with the x axis, the image at the focal plane will have an angular pattern with a single peak in  $\Phi_{LP}$  and a single valley in its diametrically opposed angle, while the intensity will continuously change in between. This suggests that for an input LP light, the CR ring will not be complete. Instead a sort of "croissant" or crescent moon shape is suggested to be shaped. A moon with its maximum pointing in the direction indicating the angle  $\Phi_{LP}$  at which the LP light was polarized. This readily suggests the device we wish to design.

# A.3. Simulating the Phenomenon

Assuming we use a focused input laser beam directed along one of the optical axes of a biaxial crystal, such that in its focal plane it has a beam waist of  $w_0$  in the absence of the crystal, we saw that equation (7) will yield the resulting electric field of the light at a distance z from the focal plane. We can generate theoretical images that a camera placed along z should register by computing first the

We have assumed the total transversal intensity  $\int_0^\infty \int_{-\pi}^{\pi} I_{CP}(q,\varphi;z) d\varphi \ q dq = \int_0^\infty 2\pi \left(|B_0(q;z)|^2 + |B_1(q;z)|^2\right) q \ dq$  (which is the  $L_2$  norm for the electric field) converges to a real number, which is to be expected since a physical input wave's transversal intensity pattern will always have a total finite intensity or "norm" (for example the Gaussian profile given next in (15) has a finite integral in q). Then, following Parseval's identity, its integral (norm) in Fourier space will also be finite, meaning that since the unitary transformation U of the crystal will preserve its norm, by reverting the Fourier transform to get  $\vec{D}$  we would still have the same finite norm or total intensity for each transversal section.

BKB integrals (8),(9) numerically and then computing the whole field  $\vec{D}(q,\varphi,z)$  and the intensity pattern  $I(q,\varphi,z) = |\vec{D}(q,\varphi,z)|^2$  for a desired input polarization  $\hat{u}_J$  with (7).

Since experimentally we can easily obtain a laser beam with a Gaussian transversal profile, we consider from now on that the input beam is so:

$$\vec{D}_0(\vec{q}) = D_0 e^{\frac{-q^2}{2}} \hat{u}_J \qquad a(k) = a_0 e^{-k^2/2} \tag{15}$$

for some real constants  $D_0, a_0$ .

With all the given, the resulting theoretical images were simulated as follows:

- 1. Let the user choose the average refractive index n, the parameters  $w_0, R_0, z$  in pixel units (where each pixel is then in our normalized units) and fix  $\hat{u}_J$  for the polarization of the input wave.
- 2. Generate a numerical Cartesian grid emulating the pixel grid of the photographic camera. Obtain the polar coordinates of each pixel of the grid.
- 3. Choose the maximum k until where we will integrate and how many points to consider within this line. It is important to take the biggest and densest possible range.
- 4. For each considered radial distance q in the image plane, compute the BKB integrals (8),(9) using a composite trapezoidal rule. For this, first numerically compute the Bessel functions over the k points for the given q and with them compute the whole integrand at each k point and q. Finally, add all the k integrand evaluations for each fixed q multiplied by the k step. This should be done in a vectorized and optimized way, for it is the bottleneck of the simulation.
- 5. Compute the displacement field at each pixel of the image  $\vec{D}$ , using the matrix equation (7) with the input Jones vector and the computed BKB integrals at each pixel.
- 6. Compute the intensity at each pixel location with the squared norm of the real part of  $\vec{D}$ . This will be what a camera at z should see.

This simulator was implemented in Python in two versions, first as a sequential vectorized calculator using the numpy library [24] and then as a batched GPU parallelized version employing both jax [25] and pytorch [42]. These can be found in the Github repository [23] with the rest of the generated code and material.

We now proceed to show some simulated results that will allow us understand more deeply the phenomenon of CR. Essentially, the generated profile has four degrees of freedom in our study:  $R_0, w_0, z$  and the input polarization  $\hat{u}_J$ . Lets see their effect.

#### Observation 1: The cone has a spatial polarization-dependent intensity distribution

We can see in Figure 2.a, for a given fixed  $R_0$ ,  $w_0$  that input CP light generates a hollow uniform ring in the focal plane z = 0, just as predicted in (A.2.1). However, if instead we input a LP light, as we do in Figure 2.b, with say, an electric field oscillating at a fixed  $\pi/2$  rad plane relative to the x axis<sup>3</sup> (oscillating along the vertical), we note that the ring lacks an intensity point and has a maximum intensity spot diametrically opposed to it. Indeed this is what we predicted would happen in (A.2.1).

To better illustrate this point, now that we have full information of the electric field, we can analyze which is the polarization of light at each point along the ring. As depicted in Figure 3, it turns out that along the ring light is found to be linearly polarized, no matter if we inputted LP or CP. Not only that, but the LP angle in each point of the ring is fixed with the crystal. Then, if we choose to input a beam with an electric field that has zero projection into a certain direction, it turns out that (a) there is no light in the point of the ring where that component should be placed, while (b) there is

 $<sup>^{3}</sup>$ We will assume all angles are relative to the x axis of the camera from now on.

maximum intensity where the LP matching the input beam's angle appears. When we input circular or randomly polarized light into the crystal, every point in the ring has light, because it is a beam that has a non-zero projection component into any orthogonal pair of axes that we could choose in the transversal profile. In fact, since this decomposition has an equal magnitude in all pair of axes, the ring appears to have an homogeneous intensity. These two findings correspond with the predictions we obtained in section (A.2.1) about the angular intensity pattern. Not only that, but in accordance with what we found there, we can verify in Figure 2 that the intensity of light is distributed along the ring in a cosinusoidal fashion for input LP, while it is constant in CP. All this suggests that the crystal acts as an continuous set of different linear polarizers spatially splitting the input beam.

The most important thing here is that given the input light is linearly polarized, with a single image of the intensity getting out of the crystal, we are able to know the LP by looking at the maximum and minimum spots.

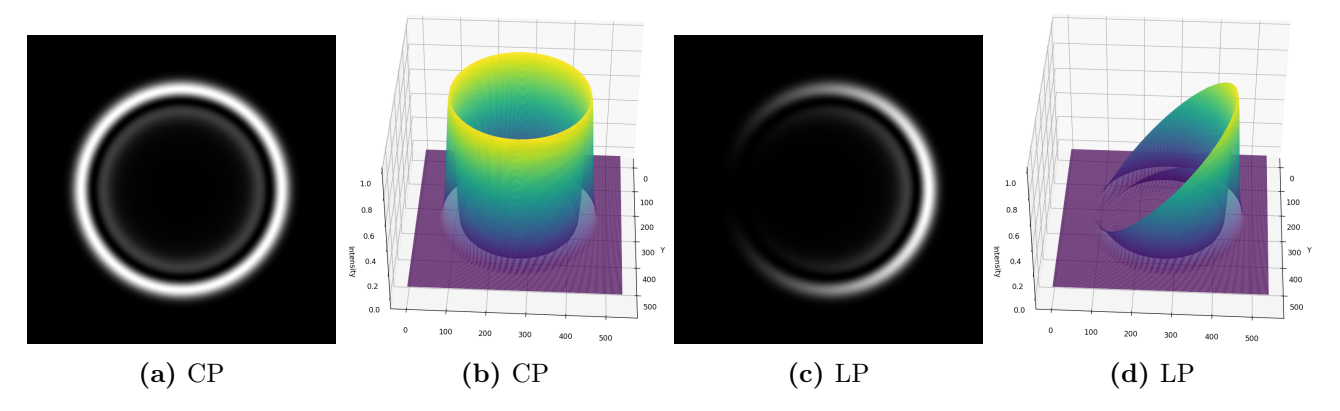


Figure 2: Simulated CR rings at z = 0,  $R_0 = 167$  pix,  $w_0 = 24$  pix for input CP in (a),(b)  $\hat{u}_J = \frac{1}{\sqrt{2}}(1,i)$  and LP in (c),(d)  $\hat{u}_J = (1,0)$ . (a),(c) represent the simulated intensity  $|\vec{D}|^2$  as a grayscale heatmap, while (b),(d) show it as a surface plot.

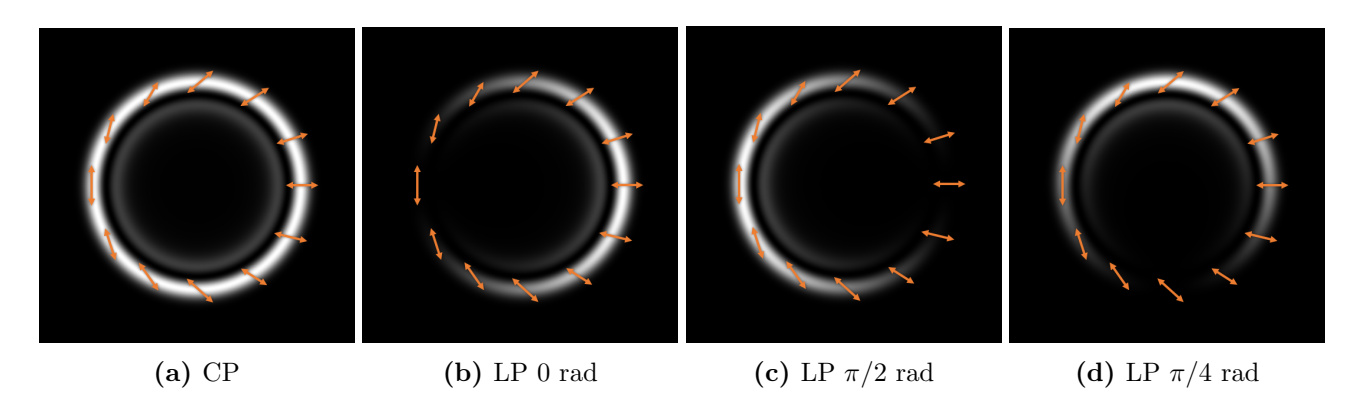


Figure 3: Simulated CR rings at z=0,  $R_0=167$  pix,  $w_0=24$  pix. Input CP in (a)  $\hat{u}_J=\frac{1}{\sqrt{2}}(1,i)$  and LP in (b),(c),(d)  $\hat{u}_J=(\cos(\Phi_{LP}),\sin(\Phi_{LP}))$  with  $\Phi_{LP}=0,\pi/2,-\pi/4$  respectively. The normalized intensity is shown as a grayscale heatmap. The arrows indicate the direction of oscillation of  $\vec{D}$  in the spatial point below them.

#### Observation 2: The $w_0, R_0$ trade-off

We can clearly see in any of the figures of this section, the dark Poggendorff ring separating the light into two rings. It is on this dark ring where Hamilton's ideal cone should be placed as we described previously. Thus, this is the ring that will define the geometrical radious  $R_0$ .

If we then modify  $R_0$ ,  $w_0$  such that the ratio  $\rho_0 = R_0/w_0$  is preserved, we can see that the image we get is the same but zoomed in or out (see Figure 6 of the full text). By fixing a certain  $R_0$ , we can see in Figure 7 of the full text, how the ring changes if we modify  $\rho_0$ . If  $\rho_0$  is made too small, the

clear segregation of the linear polarizations starts to get more diffuse. Yet, if  $\rho_0$  is too big, the ring gets very slim, which means that less pixels of the image will carry information about the ring (thus if the camera has some error per pixel, the information will get more diffuse). Then the best thing would be to choose an  $R_0$  that occupies most of the camera sensor (most pixels), without getting out of the camera plane, and by playing with  $w_0$ , choose the most convenient  $\rho_0$  in the stated trade-off.

Experimentally the problem will be that since  $R_0$  is fixed by the employed crystals' length, refractive indices and the camera's pixel density, we will only have the chance to modify  $w_0$ , which is not as helpful in trying to spread the intensity pattern through the entire camera sensor. It is this why we will employ magnifying lenses after the crystal and before the camera to make the ring of the focal point physically bigger (without altering the  $\rho_0$  parameter).

#### Observation 3: Going out of the focal plane the ring is lost

In Figure 8 of the full text, we vary where the camera is placed relative to the focal plane z=0. Clearly, the rings and their intensity distribution are most clearly visible in the focal plane (which would represent the infinity for the crystal). Going out of z=0 we loose the structure until at  $z=\pm\sqrt{4/3}\rho_0$ , known as the Raman spots, we just find a spike that barely gives us information.

# A.4. A Natural Polarimeter

The reader will have understood by now the idea that will be behind the device to measure the linear polarization of light. The CR phenomenon naturally acts as if in each point of the generated hollow ring there was a differently oriented linear polarizer, such that in a single camera image we can have the result of passing the input light beam from all the possible linear polarizers (if the resolution of the camera was infinite, of course). As a consequence, given an unknown input LP light beam, we will be able to know the angle at which the input field is oriented by looking at where the angular maximum (or minimum) intensity spot is placed. If we can process each photo fast enough, we could then measure in real time how the plane of an input LP light changes. Once this idea is in the table (as suggested already by for instance Refs. [14, 15, 13]), the main mystery to be solved would be the computer vision problem of getting the angle at which the crescent ring is oriented.

In principle this would seem to be limited to LP measurements. Yet, by dividing the input beam into two (by means of partial mirrors for example), and by employing two biaxial crystals, it is possible to build a full polarimeter that also gives all the ellipticity information. This was shown by Refs. [14, 15]. One of the arms of this device should place a quarter wave-plate before the crystal, which then using the Mueller matrices would let us know the missing polarization information.

However, following the line of reference [13] this implies complicating the design of the device, requiring double elements, from crystals to cameras, with the complication of their synchronization. Not only that, but the cost of the device would double. It turns out, for numerous interesting applications, the measurement of LP is enough.<sup>4</sup> Let us now illustrate the importance of LP measurements with several examples.

• Example in Pharmacology: There are chemical compounds (most organic compounds) that can have exactly the same elements and bonds between them and even still have two possible molecules. Just the same way as our two hands have the "same" composing bones and unions between bones, and yet they are not identical. They are mirror images. In chemistry this is called optical isomerism or enantiomerism. For example, the two molecules in Figure 4 are the same compound, with identical chemical and physical properties, except for the fact that a dissolution of one rotates the plane of polarization of an input LP light in one direction, while

<sup>&</sup>lt;sup>4</sup>In any case, the computational solutions given in this thesis are still equally applicable to such a complete polarimeter.

the other one rotates exactly the same amount in the other direction. If we have a mixture of them, where they are in equal proportions, the net LP of light does not change when crossing the dissolution. Thus, if we measure the amount of rotation of the plane of polarization, we can know the exact proportion of these enantiomers present in the mixture [16]. It turns out this is the only trivial way to measure the presence and proportion of enantiomers.

Figure 4: The Tahlidomide molecule's two enantiomers.

Their relevance mainly comes in that the enzymes in biological organisms are very selective with the conformation of their substrate molecules, to the point that typically, only one of the enantiomers of the substrate molecule of the enzyme can link to its active region. This means that it can happen, and does happen, that one of the optical isomers affects in a way, while the other one affects the organism in a very different way. The consequences in medicine are dramatic. There is this lesson given by history to the pharmaceutical industry that every organic chemistry student is told about: the Thalidomide. It was released as a drug to alleviate nausea in pregnant woman. It turned out one of the optical isomers did indeed cure nausea, but the other one disrupted the limb growth of human embryos. It is since crucial for any pharmaceutical company to constantly monitor the enantiomer proportion of their medicines, for which the only way we have is to measure the LP of light.

- Example in Experimental Chemistry: The same reasoning allows the measurement of the concentration of any particular chiral molecule in a solution, by measuring the rotation of LP light it induces [17, 18]. This method is non-invasive with the solution and can be fast enough for real time monitoring of the concentration of the chiral molecule. This is then useful for example to determine kinetic constants of chemical reactions [16].
- Example in the Food and Beverage Industry: The exact same reasoning also implies that living organisms have a preference for one of the enantiomers (for they should other-wise have two versions of many enzyme). This causes for example that only D-glucose is naturally synthesized and although it is indistinguishable in taste, L-glucose cannot be digested (and used as energy source). It is then typical in the food industry to monitor the concentration of sugar using linear polarization [60].
- Example in Astronomy: Following Refs. [19, 20], LP measurements can be used to characterize exoplanets. The light reflected from a planet, lighted by its own star, is linearly polarized by its interaction with the atmosphere, as opposed to the unpolarized light originally emitted by the star. The degree of polarization is proportional to the reflecting surface, as one of the few indicators of the size of the atmosphere over the opaque core of the planet. Not only that, but the wavelength at which the phenomenon occurs most strongly, indicates the size and thus the possible composition of the particles in the atmosphere (apart from the color of its sky). In addition, the maximum degree of polarization is achieved when the planet reflects light to Earth at a 90 degree angle. This happens when the planet is at the maximum visual separation from the star as seen from the Earth, happening twice every orbit. Therefore, the measurement of LP can even be used to characterize the period of the orbit of an exoplanet.

Among other equally interesting applications of the live measurement of LP, there are remote sensing applications [21] or the contrast enhancement of medicinal images [22]. For all of these applications and more, a cheap, portable, precise and fast LP polarimeter would definitively be a revolution.

# Part B: The Mind of the Polarimeter

In this section, we will focus our attention in the description of the developed computational solutions to determine the CR crescent ring orientation and the LP of the input light beam. Since for any reasonable measurement of LP, we need to measure it against the LP of a reference beam, we will assume in our discussion that we have two images: the crescent ring generated by the reference light beam and the one generated by the problem light beam. We will call them **the reference** and **the problem** images. Our objective is to get the relative LP angle between the incident reference and problem beams, which we will denote by  $\Delta\Phi_{LP}$ .

For notational convenience, let us define some important features of the CR crescent ring images:

- We will denote by I the intensity of light of the captured transversal section with the camera. Since the images are captured with 8 bits in the experiments, we will assume that I only takes one among 256 possible intensity values. Then, the image would be given by a function I(x,y) with the coordinates  $\vec{q} := (x,y) \in \Omega \subset \mathbb{Z}$  denoting the pixel coordinates of the image, for a certain rectangle  $\Omega = \{(x,y) \in \mathbb{Z} : 0 \le x \le W \& 0 \le y \le H\}$ , where H,W are the **height and width** of the images (the number of capturing elements of the camera in each axis of the rectangular sensor). Note that the pixel coordinate system, as typically done for computational arrays is centered in the top left corner of the image. These coordinates (x,y) represent the rows y and columns x of the image matrix.
- We will denote by  $\vec{g}_{geom}$  the **geometrical center** of the crescent ring. It is defined as the point where the center of mass of the intensity image for an input CP would lay (for the full hollow ring). It is the intersection of the central axis of the cone and the constant z plane. Since the experimental images can land, from an analyzed sample to the next one in different positions of the camera plane, it is something a **priori** we must assume to be unknown.
- We will denote by  $\vec{g}_{grav}$  the gravitational center, center of mass or **gravicenter** of the crescent ring image. It is given by:

$$\vec{g}_{grav} := \frac{\sum_{(x,y)\in\Omega} I(x,y)\vec{q}}{\sum_{(x,y)\in\Omega} I(x,y)}$$
(16)

Unlike the geometrical center, the gravicenter is trivially computable in any experimental image.

• For a generic crescent ring image, we will denote by  $\Phi_{LP}$  the angle the input light's linear polarization plane makes with the x axis of the camera's sensor, such that  $\Phi_{LP} \in (-\pi/2, \pi/2]$ . We can see from equation (14) that the angle defined as  $\phi_{CR} := 2\Phi_{LP}$  will then be the angular distance at which the peak of the CR crescent ring lands relative to the x axis of the camera sensor (assuming we center the polar coordinates in the geometric center of the ring). In particular, the relative LP angle between the problem and reference images will be given by  $\Delta\phi_{CR}/2 := (\phi_{CR_{pb}} - \phi_{CR_{ref}})/2 = \Phi_{LP_{pb}} - \Phi_{LP_{ref}} =: \Delta\Phi_{LP}$ , where the sub-indices pb, ref refer to the problem and reference rings respectively. Since typically we will compute  $\phi_{CR_{pb}}, \phi_{CR_{ref}}$  first, in order to have all relative angles  $\Delta\Phi_{LP}$  in the same branch  $(-\pi/2, \pi/2]$ , we will make sure that any  $\phi_{CR}$  angle is taken to  $(-\pi, \pi]$ . For this, Algorithm 1 is employed.

# B.1. The Computer Vision Task and the General Quandary

The computer vision problem seems simple: we have a pair of crescent-moon-like images for which we wish to know the relative angle at which they have their crest's maximum intensity points  $\Delta \phi_{CR}$ . Half this relative rotation will give us the relative linear polarization angle between the input light beams  $\Delta \Phi_{LP}$ . As derived in Part A, these CR crescent rings are expected to have very nice **geometrical properties**. Among others:

- (a) Each of them should be symmetric with respect to the axis crossing the geometric center and the maximum and minimum intensity spots along the ring. We will call this the **main (symmetry)** axis of the crescent ring.
- (b) The gravicenter  $\vec{g}_{grav}$  is aligned with the geometric center  $\vec{g}_{geom}$  along the main axis.
- (c) Following equation (14), the angular histogram obtained by radially integrating the images from the geometric center should have a squared cosine shape. Moreover, the cosine should be angularly displaced exactly double the polarization angle  $\Phi_{LP}$ .
- (d) If the problem and reference LP-s differ by  $\pi/2$  radians, that is, they are orthogonal polarizations, adding their CR rings pixel-wise, after centering both in their geometric centers, we should get a constant angular intensity profile. To see this, recalling equation (14):

$$\mathcal{I}_{\Phi_{LP}}(\varphi;z) + \mathcal{I}_{\Phi_{LP}+\pi/2}(\varphi;z) = C(z)cos^2(\varphi/2 - \Phi_{LP}) + C(z)(cos^2(\varphi/2 - \Phi_{LP} - \pi/2)$$
 (17) where using that  $cos(x - \pi/2) = sin(x)$  and  $sin^2(x) + cos^2(x) = 1$ , we get that:  $\mathcal{I}_{\Phi_{LP}}(\varphi;z) + \mathcal{I}_{\Phi_{LP}+\pi}(\varphi;z) = C(z)$ . This is a constant for a fixed  $z$ , as we wanted to prove. Its relevance is greater though. By recalling equation (11), we see  $C(z)$  is the angular profile of the complete ring generated by an input CP.<sup>5</sup> This implies an additional self-symmetry: the sum of a CR crescent ring with its  $\pi$  rad rotated version, should give a complete uniform ring.

(e) It is worth noting another consequence of the previous points: if the experimental conditions are identical (meaning  $R_0, w_0, z$  are fixed), the rings obtained by only changing  $\Phi_{LP}$  should be exact rotated versions of each other.

All these symmetries make the problem seem to be simple, and qualitatively it is. However, we are looking for the most **quantitative** result possible. To put this into context, a mildly satisfactory result would be to be able to determine the relative angles to an error within 1 degree, which are about 0.017 rad. This would imply that we are looking to classify the crescent ring image pairs in at least 360 classes. Currently sold polarimeters however, as we have seen, correctly measure polarization variations in the second decimal place in degrees (the fourth place in radians). Thus, a really satisfactory classification would involve about 36000 classes. If the images were as symmetric as theoretically predicted, then the problem would still be rather simple. However, as we will review in section (C.2), the experimental crescent rings are very noisy. So noisy that actually not even a single theoretical symmetry mentioned above really holds. This renders the quantitativeness of a generic algorithm a significant number of orders of magnitude as we will see. Even still, we will develop all sorts of algorithms based on these symmetries.

As an additional handicap, we could not have access to abundant certified ground truth LP beams, which are fundamental to know the real performance of the algorithms. They could even be useful to design models that learn to look through the experimental noise or even to mimic it. Yet, as we will see, we managed to get a few labeled samples for a final test of the algorithms. In addition, we had the advantage to be able to simulate perfect theoretical images.

#### B.2. Artificial Noise

Experimental noise had to be simulated for the theoretically perfect images in order to have labeled samples that can give us a realistic impression of how well the algorithms really perform when the

<sup>&</sup>lt;sup>5</sup>By the linear decomposition of polarization in orthogonal components this was already trivial.

theoretical symmetries are broken. Then, following the description of the experimentally found non-idealities in section (C.2), we attempt to mimic the experimental noise with the following ideas.

- 1. In order to emulate the random "bites" the crests present in experimental images (see Figures 16.b and c), we randomly modulate the image with some Gaussian shape blobs. The details of the method we designed for this can be found in the section with the same title of the full text.
- 2. In order to account for the second most notable noise type, by which the ring crests show random oscillations (see Figure 16.a), we can distort the images with a pseudo-random oscillation. The details of the developed scheme are found in the full text.
- 3. We account for Poissian noise as the last noise factor (which happens in the camera as discussed in (C.2)). For this, we consider the spoiled theoretical image so far to be the expected number of counts to be received in the x, y pixel. Then, we shot-noise the image by random sampling of a Poisson distribution with that parameter in each pixel. For details see the full text.

Example representative simulated noisy images can be found in Figure 5. Note that indeed, they are similar to the experimental noises of Figure 16.

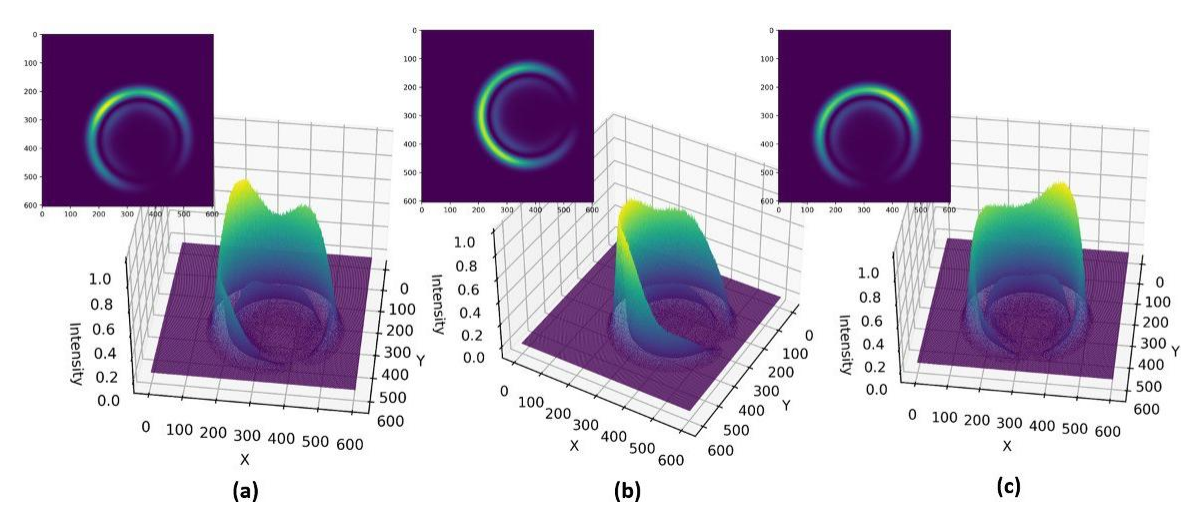


Figure 5: Representative examples of random simulated noisy images, plotted as heatmap and surface plots.

# **B.3.** The Simulated Image Datasets

The small labeled experimental image datasets of section (C.3) should only be used as a decisive benchmark. Thus, we generate several simulated image datasets, each of them with (for our purposes) an unlimited (about 1e6) number of labeled samples. For the storage of the resulting image- and label-arrays the HDF5 binary data format was employed, managed in Python by the h5py library [26].

• Mother Dataset: The numerical computation of each simulated image takes a considerable amount of time. The bottleneck is the computation of the  $B_0$ ,  $B_1$  integrals<sup>6</sup>. Once we have  $B_0$ ,  $B_1$ , CR rings for arbitrary Jones vectors can instantly be generated. In particular, it is convenient to pre-compute the matrix that in equation (7) appears getting multiplied with the Jones vector, which we will call the D matrix<sup>7</sup>, for several  $R_0$ ,  $w_0$ , z in a given grid. This is the content of the Mother Dataset. The grid of possible  $R_0$ ,  $w_0$ , z was designed around the experimentally found average parameters (a slightly wider range to test the robustness of the algorithms). It contains 115 equispaced  $R_0$  in (110, 180), 115  $w_0$  in (8, 35) and 3 z in (0, 0.05) — so few z values are considered because setting the camera in the focal plane is a task we can perform with great accuracy. Each D matrix is linked to its ground truth  $R_0$ ,  $w_0$ , z,  $\phi_{CR}$  in the dataset, which can thus be used as a look-up table in the Simulation Fit algorithms (B.9).

<sup>&</sup>lt;sup>6</sup>We did not have the chance to properly GPU parallelize the computation of the Bessel functions.

<sup>&</sup>lt;sup>7</sup>For it is the last preamble to obtain the displacement  $\vec{D}$ .

- Non Noisy Image Dataset: Using the Mother Dataset, a huge library of random simulated images was generated, both in 8 bit .png format and the HDF5 format. All images were generated without noise and with the ground truth  $\phi_{CR}$  labeling them. The images are normalized to their maximum possible value (255 for 8 bits). The objective of this dataset is to test how the algorithms perform in the most ideal of the conditions, but for random ring parameters. Note that the library contains  $R_0, w_0, z, \phi_{CR}$  of any value in the Mother Dataset's grid, even if in the actual device, this range is quite controlled.
- Noisy Image Dataset: Using the Mother Dataset, a dataset with the same features as the previous Non Noisy Image Dataset was generated, but now applying the random artificial noise to each image. The parameters of the noise were set to produce significantly noisier images than the experimental ones, since the objective of this dataset is to test the robustness of the algorithms in front of the worst-case-scenarios.
- Variant Image Dataset: A special dataset was generated to train the triplet loss embedder that we will explain in (B.7). It contains multiple different noisy versions of the same non-noisy images batched together and labeled by their common  $\phi_{CR}$  ground-truth.

# **B.4.** Preprocessing

Because the rings can appear centered quite randomly in the experimental images, in order for them to be comparable it is convenient to standardize them somehow. For this we suggest the method we named iX or Kalkandjiev standard (for it was thought by Prof. Todor K. Kalkandjiev).

• The Kalkandjiev-iX Standard: The gravicenter of the image is trivial to be computed using equation (16). Then the iX standard converts the image to a square  $(2X + 1) \times (2X + 1)$  image with the gravicenter in the center of it, with  $X \in \mathbb{N}$  pixels to the left, right, above and below. The first thing is to choose an X value such that the rings of the range captured by the camera can fit in. The procedure is to create a 2X + 1 side square blank array, where by an output-to-input strategy we set the gravicenter rounded to the nearest whole integer in the (X + 1, X + 1)-th pixel. The details can be found in Algorithm  $2^8$ . In our case, since the employed camera has a resolution of  $720 \times 540$ , we decided to use X = 302, such that the resulting image of size  $605 \times 605$  could embody any reasonable gravicenter-centered ring. Note that the rings of the iX images are tilted towards the maximum intensity direction, which is why a bit more than 540 pixels in each side were necessary.

Algorithm 2: Convert Image to Kalkandjiev-iX Standard - High Level Pseudocode

```
Given I, X
 \vec{g} \leftarrow \text{compute gravicenter } (I); 
 iX \leftarrow \text{empty array of size } [2X+1, 2X+1]; 
 \vec{l}, \vec{u} \leftarrow \vec{g} - X, \vec{g} + X + 1; 
 l\vec{b}, \vec{ub} \leftarrow \text{clip to range } [0, shape(I)] (\vec{l}, \vec{u}); 
 pad_{low}, \leftarrow l\vec{b} - \vec{l}; 
 pad_{up}, \leftarrow \vec{ub} - \vec{u}; 
 iX[ pad_{low}[0] : pad_{up}[0], pad_{low}[1] : pad_{up}[1] ] \leftarrow I[ \ \vec{lb}[0] : \vec{ub}[0], \ \vec{lb}[1] : \vec{ub}[1] ]; 
 \mathbf{return } iX
```

Now, assuming the images are set in the common iX geometry, we can try to alleviate part of the noise and try to recover some of the symmetries of the images using pre-processing techniques before feeding the  $\Delta\Phi_{LP}$  extraction algorithms. Let us describe the pre-processing techniques we implemented. We will denote by  $I_p(x,y)$  the post-processed version of I(x,y).

<sup>&</sup>lt;sup>8</sup>Note that in every Algorithm box, we will assume the arrays start indexing at 0 and the -1 index is the last element. Then, the range of indices i:j goes from i until j, including j-1 but not j.

- Normalize to Maximum Intensity: Because experimental images may be taken with different exposure times and the input laser beam's intensity might fluctuate significantly from image to image, it is important to have a way to scale the rings "vertically" (in the intensity axis) in a common manner. For some of the algorithms, like the Simulation Fit or the Relative Rotation this will be a necessity. The procedure is simple:  $I_p(x,y) = I(x,y)/max[I(x,y)]$ . It takes the image to the range [0,1]. Its application on the experimental images of Figure 16 can be seen in Figure 11 of the full text.
- Normalize to Maximum and then to Mean: The normalization to maximum is very prone to biased results when it is the maximum of the ring that has been damaged by noise (which turns out to be the case most of the times). As an alternative, we could normalize the image to its mean intensity value after being normalized to its maximum value. This should be robuster because the average intensity is harder to be corrupted than the single maximum point of the image.  $I_p(x,y) = (I(x,y)/max[I(x,y)])/mean\{I(x,y)/max[I(x,y)]\}.$
- Saturate at a Threshold Intensity: Because the information in the crests is typically very corrupted, a pre-processing that gave good results for some algorithms was to almost binarize the image. To leave only the bottom part of the image in terms of intensity. That is, to clip all the intensity values that were bigger than a certain ratio  $t \in (0,1)$  of the maximum intensity value, and then to normalize the whole to unity:  $I_p(x,y) = least[I(x,y)/max[I(x,y)], t]/t$ . It is not exactly a binarization of the image because the curves at the bottom in I (below the threshold) are still preserved, as can be seen in Figure 12 of the full text. Only very low thresholds (like t = 0.05) gave good enough results.
- Sigmoid Transformation: A smoother and differentiable version of the threshold clipping is to apply a functional transformation to each intensity value, by which the lower parts of the crest are given more weight. The sigmoid is one such transformation:  $I_p(x,y) = \frac{1}{1+exp(-k(I(x,y)/max[I(x,y)]-c))}$ . It leaves two free parameters however: the central point of the sigmoid c (analogous to the thershold) and its "slope" k. It will tend towards a strict binarization as  $k \to \infty$ . Since it is the best found method, we include an example of its application in experimental images here. See Figure 6.

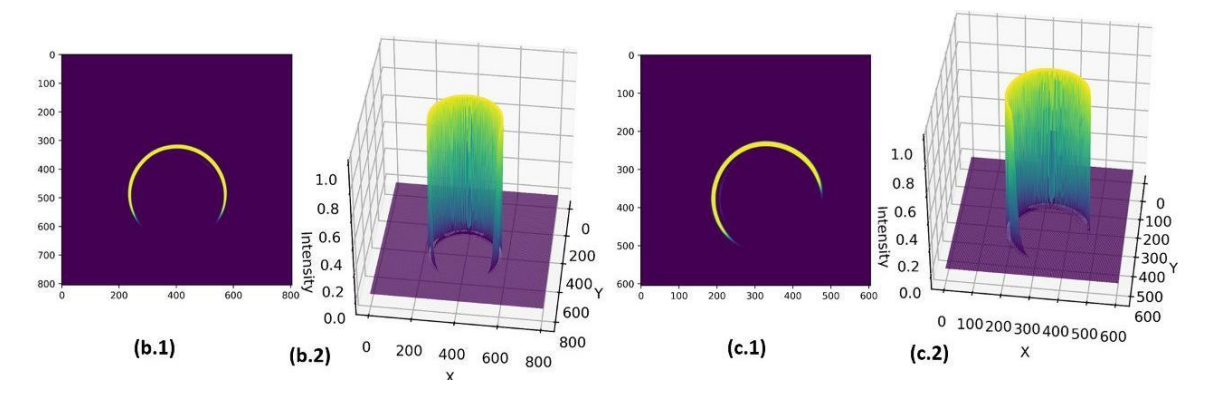


Figure 6: "Sigmoid Transformation" pre-processing applied on the experimental images of Figure 16.

• Morphological Opening: Both the threshold saturation and the sigmoid act as almost-binarizations segmentating the crescent moons. These segmentations are however performed in a global manner: without taking into account that there could be regions of the image with locally varying ranges of intensity. There could, for example, be a hole in the case of the device introducing an asymmetric background light. Then, a robuster method (that is also more computationally costly) to erase the crests of the rings, is to apply a morphological grayscale opening to the image [27]. This operation moves a sliding structuring element around the image that first erodes morphologically the image and then dilates it, getting rid of the so called "top-hats" or local maximums (which in our case are the irregular crests).  $I_p(x,y) = Dilate[Erode[I(x,y)]]$ . The size of the structuring element will determine the width of the local maximums or "hats" that will be erased. We find values between 7 and 11 pixels to be fine. See some examples in Figure 14 of the full text.

# **B.5.** Optimization Algorithms

Before jumping to the implemented algorithms that obtain  $\Delta\Phi_{LP}$ , let us describe the implemented optimizers. Most of the algorithms we designed require an optimization step to find the  $\phi_{CR}$  angle by the minimization of a certain cost function  $C(\vec{x})$  specific to the algorithm. Several of them only involve a one dimensional search space  $x \in \Gamma \subset \mathbb{R}$ , while some others involve a multidimensional search  $\vec{x} \in \Delta \subset \mathbb{R}^n$  with n > 1. Because for 1D minimization there are simple efficient algorithms, we implemented them separately, and only used the multidimensional ones when really required. In any of the cases, the cost function was a black-box function for which we do not know the analytic formula, nor we have the chance to have an explicit gradient.

- One Dimensional Optimization Algorithms: The detailed description of the implemented algorithms explaining their rationale and the pseudo-code of our implementation can be found in the full dissertation. Essentially, we implemented the well known Quadratic Fit Search [28] and the Fibonacci Ratio Search [29].
- Multidimensional Optimization: The optimizers known as the Nelder-Mead method and the Powell method were found to be properly implemented in the *scikit-optimize* library for Python [32], so we did not implement them. The description of the algorithms can be found in the full text.

# B.6. The Geometric Algorithms

We designed the algorithms of this section to explicitly exploit the geometrical properties described in (B.1) in order to let us know  $\Delta\Phi_{LP}$  from the crescent ring images. In what follows we will describe the inner workings of each one.

# B.6.1. The Relative Rotation Algorithm

One of the simplest ideas would be to use the fact that crescent rings for fixed experimental conditions, fixed  $R_0, w_0, z$ , should be exactly the same, only differing in a  $\Delta \phi_{CR}$  rotation by their geometric centers (property (e)). The key point is that if we rotate the image instead about the gravicenter, we still get a match at an angle  $\Delta \phi_{CR}$ . Then, we could displace one of the rings to align its gravicenter with the other one's and rotate it about the new gravicenter, looking for the rotation angle that minimizes the difference between the two images. See Algorithm 3 for details. The 1D minimization of the similarity between the rotated problem and unrotated reference is done using one of the algorithms of (B.4.1). For this, we must define a similarity metric to be used as cost function. In general, unless stated otherwise, we will employ for all the algorithms the mean absolute error:

$$MAE [I_1(x,y), I_2(x,y)] = \left\{ \sum_{x,y} abs(I_1(x,y) - I_2(x,y)) \right\} / \sum_{x,y} 1$$
 (18)

# Algorithm 3: The Relative Rotation Algorithm - High Level Pseudo-Code

The main complication affecting this algorithm is the fact that the noise in the experimental images does not rotate with the input beam's LP (since it is especially due to the stationary elements). Thus, the equality assumption is never really fulfilled.

#### **Affine Transformations**

Many of the algorithms employ image translations, rotations and mirror-flips. These can efficiently be performed employing matrix operations by considering the images to be in an affine space. Essentially, we will consider the plane of the images, the coordinates of which where given by x, y, is in reality a plane embedded in a 3D space of coordinates  $x, y, \tilde{z}$ , where the image is at the  $\tilde{z}=1$  plane. That is, we consider the image pixel coordinates (x,y) to be identified with (x,y,1). Then, we see that if we apply the next matrix operation to the indices (x,y,1) of the matrix:

$$\begin{pmatrix}
1 & 0 & t_1 \\
0 & 1 & t_2 \\
0 & 0 & 1
\end{pmatrix} 
\tag{19}$$

since we are moving the  $\tilde{z}$  unit vector (0,0,1) to  $(t_1,t_2,1)$ , for the image's perspective in  $\tilde{z}=1$ , we are moving its origin (0,0) to  $(t_1,t_2)$ . By the linearity of the application, we are thus translating all the pixels of the image a vector  $(t_1,t_2)$ . In  $\mathbb{R}^2$  this could not be done with linear applications, for a linear application must always send the (0,0) vector to itself.

This then allows us to compose several of these, so called affine operations, to get a single more delicate operation on the image, that  $\mathbb{R}^2$  linear applications did not allow us. For instance, it is this how we can apply a **rotation**  $\theta$  **about a point**  $(c_x, c_y)$  that is not the origin (0,0): first translate the center of rotation  $(c_x, c_y, 1)$  to the origin of the image (0,0,1) (that is, send (0,0,1) to  $(-c_x, -c_y, 1)$ ), then rotate the image about its origin (0,0,1), an angle  $\theta$  (with the expanded  $\mathbb{R}^2$  application). Finally take the center  $(c_x, c_y)$  back to its place (translate the "origin" by  $(c_x, c_y)$ ). Composing their matrices we get the operation in a single matrix:

$$rotation(\theta, c_x, c_y) = \begin{pmatrix} 1 & 0 & c_x \\ 0 & 1 & c_y \\ 0 & 0 & 1 \end{pmatrix} \begin{pmatrix} cos(\theta) & -sin(\theta) & 0 \\ sin(\theta) & cos(\theta) & 0 \\ 0 & 0 & 1 \end{pmatrix} \begin{pmatrix} 1 & 0 & -c_x \\ 0 & 1 & -c_y \\ 0 & 0 & 1 \end{pmatrix} = (20)$$

$$\begin{pmatrix}
=cos(\theta) & -sin(\theta) & -c_xcos(\theta) + c_ysin(\theta) + c_x \\
sin(\theta) & cos(\theta) & -c_xsin(\theta) - c_ycos(\theta) + c_y \\
0 & 0 & 1
\end{pmatrix}$$
(21)

Much the same way, we can obtain the affine operation for performing a **mirror flip along an** axis crossing the center  $(c_x, c_y)$ , at an angle  $\theta$  with the x axis. In  $\mathbb{R}^2$  a flip around the x axis can be done by simply flipping (0,1) to (0,-1). Then, for the arbitrary mirror flip, we could first translate the center  $(c_x, c_y)$  to the origin, rotate the image by  $-\theta$ , so we align the desired axis with the x axis, and then apply the sign flip to the y axis. By unrotating  $\theta$  and translating the "origin" back to  $(c_x, c_y)$ , we would get the desired result in the image. If we multiply their matrices (from right to left) we get all in a single affine operation:

$$mirror(\theta, c_x, c_y) = \begin{pmatrix} cos(2\theta) & sin(2\theta) & c_x(1 - cos(2\theta)) - c_y sin(2\theta) \\ sin(2\theta) & -cos(2\theta) & c_y(1 + cos(2\theta)) - c_x sin(2\theta) \\ 0 & 0 & 1 \end{pmatrix}$$
(22)

The algorithm to apply such a transformation to an image is an output to input one. First create an empty array with the same dimensions as the image: it will be the output image. Then invert the affine operation and apply it to each pixel coordinate of the output image matrix, so we know which is the (floating point) pixel of the input image that should land in each output image pixel. Typically a floating point position of the input image will be required. However, we only posses information over the integer positions. Thus, interpolation of the intensity values surrounding the floating point pixel is required. Taking for instance, the intensity value of the closest pixel is known as a nearest neighbour interpolation. A more elaborated interpolation is also possible. OpenCV's Python port [33] offers a great variety of interpolators. Thus, we heavily used it for affine operations. The ones in which we relayed more are the Lanczos [34] and the bicubic interpolation.

#### B.6.2. Registration of the Polar Coordinate Image

An alternative way to implement the idea of the previous algorithm, by which we try to register (match) the reference and problem images rotationally, would be to recast it into a translational registration problem, which has many traditional solutions. We can do this, following Refs. [37, 38], by converting the images into polar coordinates centered at their gravicenters, where one axis would now be the radial distance and the other one the angle at which each intensity value is found. By doing so, if the original images only differed by a rotation  $\Delta \phi_{CR}$ , the polar coordinate images should only differ by a translation along the angle's axis equal to  $\Delta \phi_{CR}$ .

In order to generate the polar version of the image, an output-to-input strategy, like the one explained for affine transformations, is employed. We first create the output polar image, in which we fix the output pixels in a grid of  $N_{\theta}$  angle point times  $N_r$  radial points. We then compute which would be the Cartesian coordinates (x,y) -or pixel coordinates of the original image- for each angle and radius pair. Possibly these pixel coordinates will be floating point numbers, so we will need to apply an interpolation just as in affine transformations. This time, we employ the  $warp_-polar(\cdot)$  function of the scikit-image Python library [36] for this (with a bicubic interpolation).

Once we have the polar images, we can obtain the translation necessary for the best registration using any traditional computer vision algorithm. In particular, we choose Fourier phase correlation following [37, 38]. The mathematical prove of its workings is given in the full dissertation.

```
Algorithm 4: Registration of the Polar Coordinate Image - High Level Pseudo-Code

Given I_{pb}, I_{ref}, \vec{g}_{pb}, \vec{g}_{ref}; # \vec{g}_{pb}, \vec{g}_{ref} are the gravicenters #

| polar_pb, polar_ref \( \leftarrow \) to_polar_coordinates(I_{pb}, \vec{g}_{pb}), to_polar_coordinates(I_{ref}, \vec{g}_{ref});

\[ \Delta \phi_{CR}, \Delta \text{scale} \( \leftarrow \) register using Fourier Phase Correlation (polar_pb, polar_ref);

\[ \Delta \phi_{CR} \( \leftarrow \) take to (-\pi, \pi) with alg. 1 {\Delta \phi_{CR}};

\[ \text{return } \Delta \phi_{CR}/2 \]

# It returns \Delta \Phi_{LP} #
```

In particular, we employed the sub-pixel interpolation provided by the *scikit-image* library in Python [36] for the Fourier phase correlation. This allows to get the optimal translational registration of the polar images with sub-pixel accuracy.

#### A Discarded Fourier Space Algorithm

We saw that spatially translated functions that are other-wise equivalent, have exactly equal Fourier decomposition  $\mathbf{magnitudes}$  — they will be composed of sinusoids of the same frequencies, meaning only their phases will be different. This fact, together with the fact that the Fourier decomposition of relatively rotated images will be equally rotated (since the direction of the frequency patterns, the  $\vec{k}$  directions of the plane waves, will rotate accordingly), suggests an additional algorithm. We could convert the reference and problem images, which need not have their gravicenters centered in the same pixel, to Fourier space, leave only their magnitudes and apply the rotational registration to the Fourier magnitudes themselves. For this we could use again, a 1D optimization algorithm or yet an additional Fourier transform to compute the Phase cross correlation. This was in reality the algorithm suggested by Refs. [37, 38]. However, we found that manipulating the non-smooth Fourier space magnitudes was very error-prone.

# B.6.3. The Kalkandjiev-Rotation Algorithm

Perhaps a more robust option than relaying in the strict similarity between the reference and problem images is to find the angles  $\phi_{CR_{pb}}$  and  $\phi_{CR_{ref}}$  that each ring separately takes with the x axis of the camera, to only afterwards compute their difference  $\Delta\phi_{CR} = \phi_{CR_{pb}} - \phi_{CR_{ref}}$ . In favour of the previous algorithms, if noise affects equally to both images, taking directly a measure of their relative distance would be beneficial. However, as we have mentioned, the noise pattern does not rotate with  $\phi_{LP}$ , so

the benefit melts at its core. This is why the rest of the algorithms follow the approach of looking for  $\phi_{CR_{pb}}$  and  $\phi_{CR_{ref}}$  as independent entities (allowing the computation of relative LP even between different experimental conditions, where rings are not assumed to be equal).

One of the first algorithms we thought of turns out to be of this kind. It was suggested by Prof. Todor K. Kalkandjiev. It is based on the observation that if we mirror flip a crescent ring image in the horizontal axis aligned with its gravicenter, we get an image that if we start rotating along its gravicenter, will exactly match the original image when we rotate it  $2\phi_{CR}$ . In reality the match will not be exact. It would be exact if the crescent ring is exactly symmetrical about its main symmetry axis. Experimental images do not satisfy it, yet, a match for an angle far from  $2\phi_{CR}$  is not feasible even in the presence of moderate noise. The implemented approach is detailed in Algorithm 5. We have a 1D optimization problem for the similarity function between the original image and its rotated mirror image in the x axis. The similarity once again is chosen to be (18).

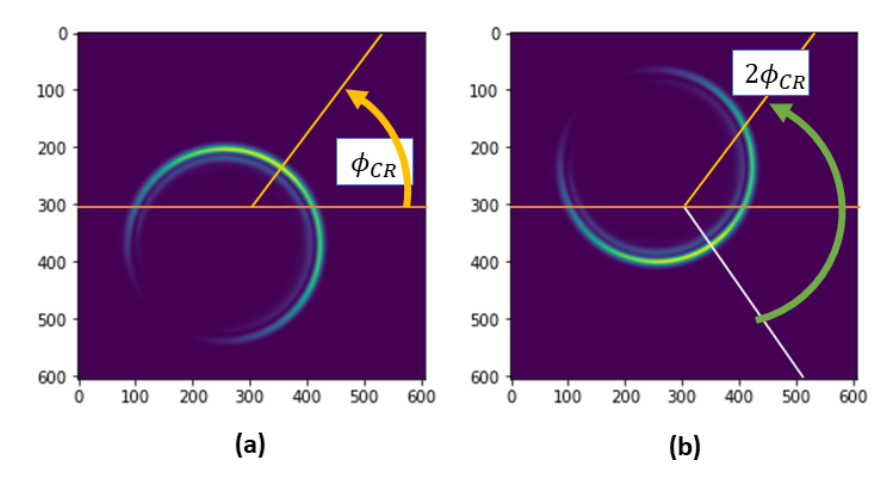


Figure 7: (a) Experimental crescent ring image indicating  $\phi_{CR}$ . (b) The image in (a) mirror flipped in the axis crossing the gravicenter. A  $2\phi_{CR}$  rotation should make it almost equal to (a). Note that what we end up comparing at that angle is each half along the main axis, where they should be symmetric.

```
Algorithm 5: The Kalkandjiev-Rotation Algorithm - High Level Pseudo-Code. To get \Delta\Phi_{LP} use I \in \{I_{pb}, I_{ref}\}, to get \phi_{CR}, \phi_{CR} then \Delta\Phi_{LP} = (\phi_{CR} - \phi_{CR})/2.
```

A problem this algorithm (as well as some of the next ones) presents is that the obtained optimal relative rotation can equally likely turn out to be  $\phi_{CR}$  (the angle to the crest's hill), or the angle to where the minimum intensity should be (the valley of the crest), which is  $\pi$  rad apart from  $\phi_{CR}$ . Then, to obtain the correct value of  $\Delta\Phi_{LP}$ , we need to compute the difference employing for both rather  $\phi_{CR}$  or  $\phi_{CR} \pm \pi$ . Therefore, once we have obtained the angle  $\varphi$ , which can be anyone in  $\{\phi_{CR}, \phi_{CR} + \pi\}$ , we need a post-process to distill say,  $\phi_{CR}$ . We do this employing Algorithm 6.

Essentially, the trick is to notice that which-ever is  $\varphi$ , it equally indicates the main symmetry axis. Thus, its orthogonal axis can be described by  $\varphi + \pi/2$ , whichever it was in  $\{\phi_{CR}, \phi_{CR} + \pi\}$ . This orthogonal axis to the main symmetry axis is  $y = g_y + tan(\varphi + \pi/2)(x - g_x)$ , where  $(g_x, g_y) = \vec{g}_{grav}$ . Knowing this, we can define an index mask that indicates which indices of the image are above the

line and which ones are below the line. With it, we add up the pixel intensities for the ones laying above and the ones laying below the asymmetric axis and compute their difference (up minus down)  $\Delta ring$ . If the difference is positive, then the ring maximum is above this axis and  $\phi_{CR}$  lays in  $(0, \pi)$ , else, it will be in  $(-\pi, 0)$ .

**Algorithm 6:** Knowing  $\varphi \in \{\phi_{CR}, \phi_{CR} - \pi\}$  **obtain**  $\phi_{CR}$  - High Level Pseudocode

```
Given \varphi, I, \vec{g}_{grav}:
    if \varphi == 0 or abs(\varphi) == \pi then
        \varphi \leftarrow \varphi + 10^{-12};
                                               # Not ideal, but will never get such a good precision #
    \Delta ring \leftarrow \text{given orthog. axis ang. to main ax. get } I \text{ diff. at each side}(\varphi + \pi/2, I, \vec{g}_{grav});
    if \Delta ring > 0 then
                                                                                         # \phi_{CR} is the one in (0,pi) #
         if \varphi < 0 then
             return \varphi + \pi
         else
           \mid return \varphi
    else
         if \varphi > 0 then
           | return \varphi - \pi
         else
             return \varphi
```

# B.6.4. The Mirror Flip Algorithm

This is another algorithm that exploits the supposed self-symmetry of the crescent ring along its main axis (geometric property (a)). Using affine operation (22), we can compute the result of taking a mirror flip of an image along an arbitrary axis crossing the point  $(c_x, c_y)$  at an angle  $\theta$ . Then, since the crescent rings are symmetric along their main axis, which is the axis crossing the gravicenter  $\vec{g}_{grav}$  (known) and oriented at an angle  $\phi_{CR}$ , we can 1D search for the angle at which to apply the mirror flip such that the result is most similar to the original image (this time the minimum is bounded in  $[-\pi/2, \pi/2)$ , since we look for an axis). The followed procedure is described in Algorithm 7. This algorithm as well, only provides us  $\phi_{CR}$  up to  $\pi$ , so it requires the post-processing technique of Algorithm 6.

```
Algorithm 7: The Mirror Flip Algorithm - High Level Pseudo-Code
To get \Delta\Phi_{LP} use I \in \{I_{pb}, I_{ref}\}, to get \phi_{CR}, \phi_{CR} then \Delta\Phi_{LP} = (\phi_{CR} - \phi_{CR})/2.
```

```
Def C(phi; I, \vec{g}_{grav}, similarity(\cdot, \cdot))

| mirror \leftarrow affine mirror flip on custom axis(I, at angle=phi, axis\_center= \vec{g}_{grav});

return -similarity(mirror, I)

Given I, C, I, \vec{g}_{grav}, similarity(\cdot, \cdot), \phi_{min} := -\frac{\pi}{2}, \phi_{max} := \frac{\pi}{2}

| I \leftarrow iX \text{ standard } (I);

| w \leftarrow \{I, \vec{g}_{grav}, \text{ similarity}(\cdot, \cdot)\};

| x \leftarrow 1D \text{ minimum Search } (C(\cdot; w), \phi_{min}, \phi_{max});

| \phi_{CR} \leftarrow \text{ get angle to crest hill with alg. } 6 (| x/2 |);

return (take to (-\pi, \pi) with alg. 1 \{\phi_{CR}\})

# It returns \phi_{CR} #
```

#### B.6.5. The Gravicenter Regression Algorithm

This is an improvement of another idea suggested by Prof. Kalkandjiev. Let us take a circular mask of radius r around the gravicenter  $\vec{g}$  and erase the pixels outside the circle. The gravicenter of the masked image,  $\vec{g}_r$ , will land in a different spot as a function of the radius of the mask. If the radius is so small that no pixel with ring information is inside, the gravicenter will lay in the center of the image, where the whole image gravicenter was  $\vec{g} \simeq \vec{g}_r$  (assuming the image is iX standardized). If we make the circle so big as to include the whole crescent ring, then the mask-gravicenter will lay again around

the gravicenter of the whole image  $\vec{g} \simeq \vec{g_r}$ . However, for intermediate radii the gravicenter will land in different spots, all theoretically within the main symmetry axis. This is because the circle always takes a symmetric piece of each half of the ring within it. Because  $\vec{g}$  is tilted towards the maximum intensity of the crescent ring, as r increases the mask will first intersect only with the side of maximum intensity. Therefore,  $\vec{g_r}$  will get even closer to that side of the ring than  $\vec{g}$ . It will keep approaching as r increases, until at a certain  $r_0$ , the circle mask intersects with enough of the other side of the ring, to make  $\vec{g_r}$  move back towards  $\vec{g}$ . It turns out the  $r_0$  point lays exactly in the Poggendorff dark ring for a ring with big enough  $\rho_0$ .

The magnificent idea proposed by Prof. Kalkandjiev was that we could take the point  $\vec{g}_{r0} = (g_x^{(r0)}, g_y^{(r0)})$ , which is the furthest one from  $\vec{g} = (g_x, g_y)$ , to compute their relative vector  $\vec{G} := \vec{g}_{r0} - \vec{g}$ , which will have a magnitude  $r_0$  and an angle  $\phi_{CR}$ , because all  $\vec{g}_r$  lay along the main axis<sup>9</sup>. Then not only we get directly  $\phi_{CR} = tan^{-1} \left( \frac{g_y^{(r0)} - g_y}{g_x^{(r0)} - g_x} \right)$ , but we know  $r_0$ , the distance from the gravicenter to the Poggendorff dark ring along the main axis. He suggested that this should be related by a simple relation with the distance to the geometric center  $R_0$  along the same axis, which if found,  $R_0(r_0)$  would provide us an estimate of the geometrical center  $\vec{g}_{geom}$ . At the same time, this would give us access to more advanced algorithms to refine  $\phi_{CR}$ .

However, it turns out there is not a trivial relation between  $R_0$  and  $r_0$  if we allow  $w_0$ ,  $R_0$ , z to vary. This means, we could train a function to predict  $R_0(r_0)$ , but then we would loose the elegance of the method. In addition, yes, it is true that to compute  $\vec{G}$ ,  $\vec{g}_{r0}$  is the most convenient one of the  $\vec{g}_r$ : since it is the furthest one form  $\vec{g}$ , it is the one that the same perturbation in position will affect the least to the indicated angle  $\phi_{CR}$ . Nevertheless, it could happen that precisely at radious  $r_0$  the circle starts to take in very noisy parts of the ring. Why then not use just the previous r-s? Well, because it could happen that it is the inner part that is noisier. Then why not wait for the mask to take as much of the ring as possible to compensate the noise?

Following this criticism, we can give a more holistic version of the algorithm. We can use all the  $\vec{g_r}$ , each of which is an estimate of a point on the main axis, to fit a line by a least squares or a RANSAC [41] method. From the fitted line y = a + bx, which should represent the main symmetry axis, we can compute  $\phi_{CR}$  up to  $\pi$  with  $tan^{-1}(b)$ . Then, Algorithm 6 would end up deciding  $\phi_{CR}$ . The approach is summarized in Algorithm 8.

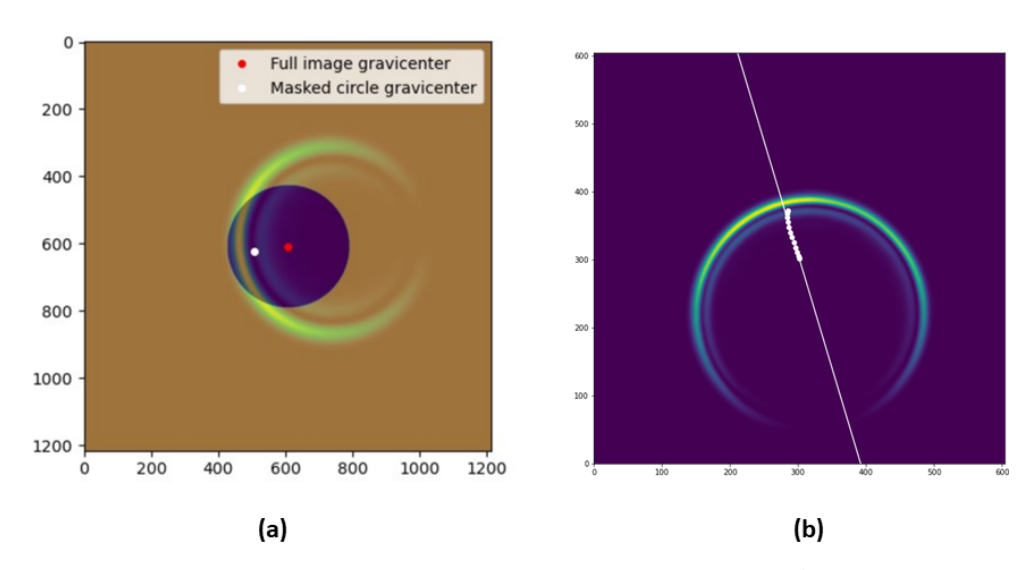


Figure 8: (a) A problem experimental crescent ring with the  $r_0$  mask over it. The  $\vec{G}$  vector is the one joining the two gravicenters. (b) Another experimental image, showing all the  $\vec{g}_r$  as white dots. The white line is the linear fit estimating the main axis obtained with them.

<sup>&</sup>lt;sup>9</sup>He called this vector  $\vec{G}$  the *gradient vector*, because it somehow points in the direction of steepest intensity surface increase. Thus the original name of the algorithm was the Gradient algorithm.

Algorithm 8: The Gravicenter Regression Algorithm - High Level Pseudo-code To get  $\Delta\Phi_{LP}$  use  $I\in\{I_{pb},I_{ref}\}$ , to get  $\phi_{CR}$ ,  $\phi_{CR}$  then  $\Delta\Phi_{LP}=(\phi_{CR}-\phi_{CR})/2$ .

```
Given I, \vec{g}_{grav}, N_r, r_{min}, r_{max}:

r_s \leftarrow \text{equispaced grid of } N_r \text{ points in } [r_{min}, r_{max}];
\mathfrak{r}(x,y) \leftarrow \text{array giving the radial distance from } (x,y) \text{ in } I(x,y) \text{ to } \vec{g}_{grav};
\vec{g}_r s \leftarrow \text{empty } [N_r+1, 2] \text{ matrix of floats};
\mathbf{for } k \in \{0, 1, ..., N_r - 1\} \mathbf{do}
\mid \vec{g}_r s[k, :] \leftarrow \text{compute gravicenter } (I[\mathfrak{r}(x,y) < r_s[k]]);
\mathbf{end}
\vec{g}_r s[-1, :] = \vec{g}_{grav};
a, b \leftarrow \text{least square or RANSAC fit } y = a + bx \text{ to observed } \{(x_k, y_k)\}_k = \{\vec{g}_r s[k, 1], \ \vec{g}_r s[k, 0]\}_k;
\varphi \leftarrow \text{tan}^{-1}(b);
\phi_{CR} \leftarrow \text{get angle to crest hill with alg. } 6 (\varphi);
\mathbf{return } (\text{take to } (-\pi, \pi) \text{ with alg. } 1 \{\phi_{CR}\})

# It \mathbf{returns } \phi_{CR} #
```

# B.6.6. The Bimodal Histogram Algorithm

We do not have an analytic expression for the angular distribution of the intensity if we center the polar node in the gravicenter  $\mathcal{I}(\theta; \vec{g}_{grav})$ . For the geometric center we do have it: by equation (14), it is a squared cosine. Yet, since the gravicenter is tilted towards the maximum intensity spot along the main axis and the ring should be symmetric about such an axis, the angular profile about the gravicenter still has an interesting shape. It looks like a symmetric bimodal distribution. There are two hills that symmetrically get close to each other with a slight depression exactly in the maximum intensity angular spot and a deep valley reaching 0 intensity in the minimum intensity angular spot. See Figure 9. This makes  $\mathcal{I}(\theta, \vec{g}_{grav})$  a periodic function if  $\theta \in \mathbb{R}$ , with two symmetry points within each period: one will indicate  $\phi_{CR}$ , the other one  $\phi_{CR} \pm \pi$ .

We could then calculate the image in polar coordinates, centered in the gravicenter, integrate the radial part and get the angular profile  $\mathcal{I}(\theta, \vec{g}_{grav})$ . Finally, looking for the point offering biggest symmetry could work to get  $\phi_{CR}$  up to  $\pi$ . Yet, this is a poorer version of say the Mirror flip algorithm, since we loose detail of the radial part, which could be critical in the matching. In addition we relay completely in the strict symmetry property around a single point.

A more holistic algorithm perhaps, is to only assume that the angular histogram  $\mathcal{I}(\theta, \vec{g}_{grav})$  represents the density of two modes, which need not have the same standard deviation properties, but such that there is a particular angle  $\phi_{CR}$  for which they are best separated. This could be measured by the average intra-mode variance. Given a boundary t and considering the angular nodes  $\{\theta_k\}_{k=0}^{N_{\theta}}$ , we define the mean and variance of each mode as:

$$\mu_{1}(t) = \frac{1}{\sum_{k=0}^{k:\theta_{k}=t} \mathcal{I}(\theta_{k}; \vec{g}_{grav})} \sum_{k=0}^{k:\theta_{k}=t} \theta_{k} \mathcal{I}(\theta_{k}; \vec{g}_{grav}) \qquad \mu_{2}(t) = \frac{1}{\sum_{k:\theta_{k}=t}^{N_{\theta}} \mathcal{I}(\theta_{k}; \vec{g}_{grav})} \sum_{k:\theta_{k}=t}^{N_{\theta}} \theta_{k} \mathcal{I}(\theta_{k}; \vec{g}_{grav})$$
(23)

$$var_{1}(t) = \frac{\sum_{k=0}^{k:\theta=t} (\theta_{k} - \mu_{1})^{2} \mathcal{I}(\theta_{k}; \vec{g}_{grav})}{\sum_{k=0}^{k:\theta=t} \mathcal{I}(\theta_{k}; \vec{g}_{grav})} \qquad var_{2}(t) = \frac{\sum_{k:\theta=t}^{N} (\theta_{k} - \mu_{2})^{2} \mathcal{I}(\theta_{k}; \vec{g}_{grav})}{\sum_{k:\theta=t}^{N} \mathcal{I}(\theta_{k}; \vec{g}_{grav})}$$
(24)

Then, we can define an average intra-mode variance, following the Otsu intra-class variance [39], as:

$$var(t) = \frac{\sum_{k=0}^{k:\theta=t} \mathcal{I}(\theta_k; \vec{g}_{grav})}{\sum_{k=0}^{N} \mathcal{I}(\theta_k; \vec{g}_{grav})} var_1(t) + \frac{\sum_{k:\theta=t}^{N} \mathcal{I}(\theta_k; \vec{g}_{grav})}{\sum_{k=0}^{N} \mathcal{I}(\theta_k; \vec{g}_{grav})} var_2(t)$$
(25)

The scheme would then be to look for the boundary angle t separating the modes that minimizes the average intra-mode variance (25). This is resilient to asymmetrically noisy crests assuming that the gravicenter (about which we compute the angular histogram) is still aligned with the geometric center at  $\phi_{CR}$ . The method is isomorphic to the Otsu algorithm [39] employed to find the optimal binarization threshold in images that are assumed to have a bimodal histogram.

We realize however that yet an additional consideration must be taken. The angular histogram plots are only computed for a single fixed period  $\theta \in [-\pi, \pi]$  in a finite array. As can be seen in Figure 9, this means that as a function of which was  $\phi_{CR}$ , we will have our ideal plot where to apply the algorithm shifted. We can solve this as follows: each s shifted version of the histogram will have its own minimum intra-class variance threshold  $t^*(s)$ . This optimal threshold will have the minimum intra-class variance when the histogram is exactly shifted by an angle  $s^* \in \{\phi_{CR}, \phi_{CR} \pm \pi\}$ , leaving a symmetric histogram plot. In fact, in that moment,  $t^*$  will also indicate the main axis  $t^*(s^*) \in \{\phi_{CR}, \phi_{CR} \pm \pi\}$ . Therefore, we have a nested 1D optimization problem by which we look for the histogram shift s that gives the optimal threshold  $t^*(s)$  of minimum intra-class variance. The shift for the minimum  $s^*$  and the minimum variance threshold within it  $t^*(s^*)$ , can both be used to get  $\phi_{CR}$  (up to  $\pi$ ).

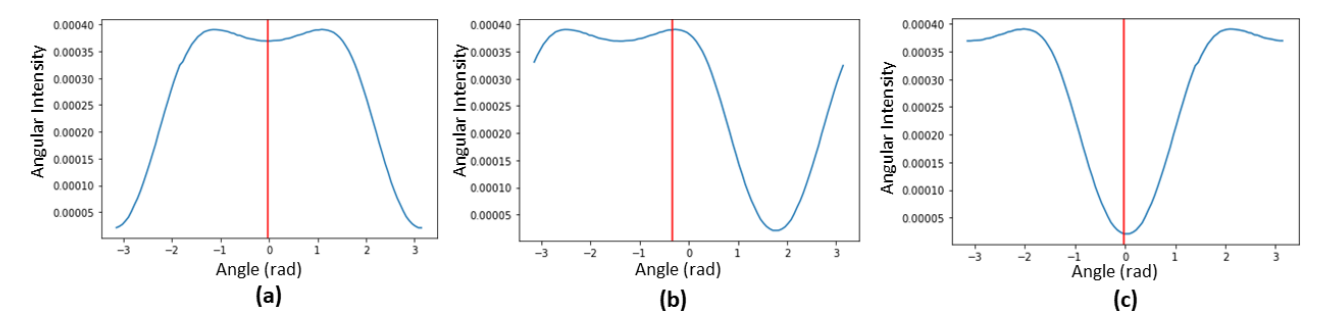


Figure 9: Angular histograms with the gravicenter as polar center. They show a red line indicating the minimum intra-mode variance threshold. They are shifted versions of the histogram of a same image. (a) and (c) show the shifts offering the minimum minimum intra-mode variance, while (b) shows an intermediate one. Note that in the optimal shifts, the optimal thresholds will always be found around the middle of the plot. When tracing back this angle by the shift, it will give  $\phi_{CR}$  up to  $\pi$ . The shift itself should also give  $\phi_{CR}$  up to  $\pi$ .

Algorithm 9: The Bimodal Histogram Algorithm - High Level Python Pseudo-code To get  $\Delta\Phi_{LP}$  use  $I \in \{I_{pb}, I_{ref}\}$ , to get  $\phi_{CR}$ ,  $\phi_{CR}$  then  $\Delta\Phi_{LP} = (\phi_{CR} - \phi_{CR})/2$ .

```
Def get min variance the shold (\vec{h}, \vec{\theta}s):
     w1 \leftarrow \text{cumulative sum } (\vec{h});
                                                                        # returns a vector: entry k is \sum_{j=0}^{k} \vec{h}[j] #
     w2 \leftarrow \text{flip order (cumulative sum (flip order } (\vec{h})));
     \vec{\mu_1}s \leftarrow \text{cumulative sum} (\vec{h} * \vec{\theta}s) / w1;
                                                                          # prod. * and div. / are element-wise #
     \vec{\mu_2}s \leftarrow \text{flip order (cumulative sum(flip order}(\vec{h}*\vec{\theta}s))/w2);
     vars \leftarrow w1[:-1] * w2[1:] * (\vec{\mu_1}s[:-1] - \vec{\mu_2}s[1:])^2;
     k_{min} \leftarrow \operatorname{argmin}(vars);
     return \vec{\theta}s[k_{min}], \ vars[k_{min}];
                                                             # returns min var threshold angle t^* and var(t^*) #
Given I, \vec{g}_{grav}, N_{\theta} N_r:
     I_{polar} \leftarrow \text{to polar coordinates}(I, \vec{g}, N_{\theta}, N_r);
                                                                                        # N_{	heta} angular pts N_{r} radial pts #
     \vec{h} \leftarrow \text{sum components along } r's axis (I_{polar});
                                                                                              # angular histogram about \vec{q} #
     \vec{\theta}s \leftarrow \text{integers array } (0, 1, ..., N_{\theta} - 1);
     t_{opt}s, var_{opt}s \leftarrow two empty arrays of length s_{max} - s_{min};
     for k \in \{0, 1, ..., s_{max} - s_{min} - 1\} do
          \vec{h}_{shifted} \leftarrow \text{concatenate } (\vec{h}[s_{min} + k :], \vec{h}[: s_{min} + k]);
          t_{opt}s[k], var_{opt}s[k] \leftarrow \text{get min variance threshold } (\vec{h}_{shifted}, \vec{\theta}s);
     end
     k_{min} \leftarrow \operatorname{argmin}(var_{opt}s);
     min\_var\_t\_shifted \leftarrow t_{opt}s[k_{min}];
                                                                         # t^* of min var(t^*) but for shifted frame #
                                                                                  # the shift in \vec{h} to get min var(t^*) #
     min\_var\_shift \leftarrow k_{min} + s_{min};
     aux \leftarrow (min\_var\_t\_shifted//(N_{\theta} - min\_var\_shift)) > 0; # // is integer division #
     min\_var\_t \leftarrow min\_var\_t\_shifted + min\_var\_shift - N_{\theta} \cdot aux;
                                                                                                              # t^* of min var(t^*) #
     \phi_{CR} \leftarrow min\_var\_t \cdot 2\pi/N_{\theta};
                                                             # this should also be \phi_{CR}, but \phi_{CR1} is bettter #
     \phi_{CR} \leftarrow min\_var\_shift \cdot 2\pi/N_{\theta};
     return (take to (-\pi, \pi) with alg. 1 \{\phi_{CR}\})
                                                                                                                # It returns \phi_{CR} #
```

The implemented scheme is described in Algorithm 9. Following it, we first run a gross search for an estimate of the optimum shift  $s^*$  and then zoom-in around it to perform a brute-force search of the actual optimum. It was done this way instead of using a nested 1D optimization, for each brute force minimum variance search  $t^*(s)$  was found to be easily vectorizable (see the function in Algorithm 9).

# B.6.7. The Blazquez Algorithm

The following algorithm was thought by Carles Blazquez, a good classmate and a great physicist. Let us define J(x,y) as the crescent ring image pixel-wise added with a  $\pi$  rad rotated version of itself:  $J(x,y) := I(x,y) + Rot_\pi about_{\vec{g}} [I(x,y)]$ . Then, the essential idea behind the algorithm is that if we rotate J(x,y) by  $\pi/2$  rad, the resulting image will be exactly the same as J(x,y) only if the rotation center  $\vec{g}$  was chosen to be the geometric center of the ring  $\vec{g}_{geom}$ . This is because by the symmetry (d) in the list in (B.1), adding a crescent ring image and its  $\pi$  rotated version about  $\vec{g}_{geom}$ , we get the hollow ring we would have got if the input was CP. Then, this hollow ring of constant angular profile will naturally be the same as its  $\pi/2$  rotated version, and actually any other rotation of itself. See Figure 10.

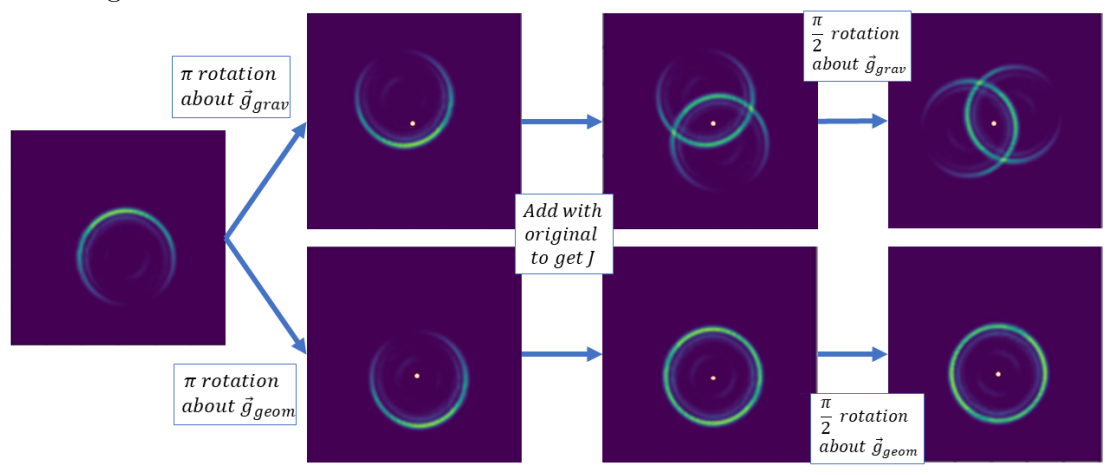


Figure 10: Schematic depiction of the construction of J choosing  $\vec{g}_{grav}$  or  $\vec{g}_{geom}$  as rotation centers.

If we only looked for J(x,y) directly being a hollow uniform ring, we would be asking the ring to be symmetric with respect to the main axis, just like with the Mirror algorithm. However, the Blazquez algorithm is more general since when we ask it to be at the same time equal to the  $\pi/2$  rotated version, we are pair-wise comparing each pair of fourth parts of the ring (see Figure 10). Thus it will be robuster to noise that breaks the strict symmetry about the main axis.

```
Algorithm 10: The Blazquez Algorithm - High Level Pseudo-code To get \Delta\Phi_{LP} use I\in\{I_{pb},I_{ref}\}, to get \phi_{CR}, \phi_{CR} then \Delta\Phi_{LP}=(\phi_{CR}-\phi_{CR})/2.

Def C_{Blz}(\ c_x,\ c_y;\ I,\ similarity(\cdot,\ \cdot)\ ): # MAE (18) good similarity for this # |\ J\leftarrow I+ {\rm rotate}\ \pi\ {\rm around}\ (\ I,\ (c_x,\ c_y)\ ); return -similarity(\ J,\ {\rm rotate}\ \pi/2\ {\rm around}\ (\ J,\ (c_x,\ c_y)\ ) Given I,\ \vec{g}_{grav},\ similarity(\cdot,\cdot): |\ w\leftarrow\{\ I,\ similarity(\cdot,\cdot)\ \}; |\ \vec{g}_{geom}\leftarrow 2{\rm D}\ {\rm min.\ Search} |\ (C_{Blz}(\cdot,\cdot;w),\ (c_{x\ min},c_{x\ max})=(0,\ width(I)),\ (c_{y\ min},c_{y\ max})=(0,\ height(I))\ ); |\ (G_x,G_y)\leftarrow\vec{g}_{grav}-\vec{g}_{geom}; |\ \phi_{CR}\leftarrow {\rm tan}^{-1}(G_y/G_x); return (take to (-\pi,\pi) with alg. 1\ \{\phi_{CR}\}) # It returns \phi_{CR} #
```

In fact, perhaps the most precise of the algorithms in the work could be a variant of Blazquez's algorithm, in which the minimized metric in the 2D search for  $\vec{g}_{geom}$  is not the difference between J(x,y) and the  $\pi/2$  rotated J, but the differences between J and a range of  $\theta_k$  rotations of J. Each additional angle  $\theta_k$  we added would make the algorithm each time more holistic, allowing to absorb

noises in the crests of the generated hollow ring when the rotations are made about  $\vec{g}_{geom}$ . This algorithm however is left as a future work if Blazquez's algorithm turns out to perform well.

The current implementation, following Blazquez's original idea is listed in Algorithm 10. One thing is left yet. What we obtain with the algorithm so far, is the geometric center  $\vec{g}_{geom}$ . Then the trivial way to obtain  $\phi_{CR}$  from it is by using that the gravicenter  $\vec{g}_{grav}$  is aligned with the geometric center along the main axis. By computing the relative vector along the axis  $\vec{G} = (G_x, G_y) := \vec{g}_{grav} - \vec{g}_{geom}$  we could then get  $\phi_{CR} = tan^{-1}(G_y/G_x)$ .

# B.6.8. The Squared Cosine Fit Algorithm

This is another algorithm to look for the geometric center and in the way find  $\phi_{CR}$ . We know that the angular histogram of a CR crescent ring image will only have a cosine squared shape given by equation (14) when the angular intensity profile  $\mathcal{I}(\theta; \vec{c})$  is computed using as polar center  $\vec{c} = (c_x, c_y)$  the geometrical center of the ring  $\vec{g}_{geom}$ . We can parameterize this cosine square following (14) as:

$$\mathcal{I}(\theta; \vec{c} = \vec{g}_{geom}, C, \Phi_{LP}) = K + C\cos^2(\theta/2 - \Phi_{LP})$$
(26)

where we included an additional degree of freedom  $K \in \mathbb{R}$  to account for baseline noise.

This means we could make a 2D search in the possible polar center space  $\vec{c} \in \Omega$  computing angular histograms at each point and fitting a cosine square of parameters  $K, C, \Phi_{LP}$  until the fitting error is minimum. Alternatively the followed approach could be to make a 4D search in the whole  $\vec{c}, K, C, \Phi_{LP}$  space. However, the least square error cosine square fit can be done "exactly" within each  $\vec{c}$ . To do this, we first use the identity  $\cos^2(x) = (1 + \cos(2x))/2$  and then the relation employed in (A.1.1) – in the full text – relating a de-phased cosine with the sum of a sine and a cosine, to get:

$$K + C\cos^2(\theta/2 - \Phi_{LP}) = E + A\cos(\theta) + B\sin(\theta)$$
(27)

with  $C/2 = \sqrt{A^2 + B^2}$ ,  $\Phi_{LP} = tan^{-1}(B/A)$  and K + C/2 = E. Then, given  $\vec{c} \in \mathbb{R}^2$ , we compute the angular histogram and find the fit that produces the least squared errors, which as proved in detail in the full text, is given by the so called "normal equation" solution, which is a classical algorithm [40].

If we build a cost function that gives, as a function of  $\vec{c}$  (the polar center of the angular plot), the fit error of the least-square-error cosine, the cost will be minimum when  $\vec{c} = \vec{g}_{geom}$ . Then, once we know A, B for  $\vec{c} = \vec{g}_{geom}$  we can immediately obtain  $\Phi_{LP}$  as  $\Phi_{LP} = tan^{-1}(B/A)$ . See Algorithm 11.

Algorithm 11: The Squared Cosine Fit Algorithm - High Level Pseudo-Code To get  $\Delta\Phi_{LP}$  use  $I\in\{I_{pb},I_{ref}\}$ , to get  $\Phi_{LP},\Phi_{LP}$  then  $\Delta\Phi_{LP}=\Phi_{LP}-\Phi_{LP}$ .

```
Def C_{csf}(c_x, c_y; I, \vec{\theta_s}, N_\theta, N_r, er)
      I_{polar} \leftarrow \text{to polar coordinates } (I, (c_x, c_y), N_\theta, N_r);
                                                                                                     # N_{	heta} angular pts N_{r} radial pts #
      \vec{\mathcal{I}} \leftarrow \text{sum components along } r\text{'s axis } (I_{polar});
      H \leftarrow \text{matrix with } N_{\theta} \text{ rows, where k-th row is } [1, \cos(\vec{\theta}s[k]), \sin(\vec{\theta}s[k])];
      \vec{x}_{opt} \leftarrow \text{solve } \vec{x} = (E, A, B) \text{ for } \mathbf{H}^t \mathbf{H} \vec{x} = \mathbf{H}^t \vec{\mathcal{I}} \text{ with LU decomposition;}
      if er = True then
            return Euclidean norm of \vec{\mathcal{I}} - H\vec{x}_{opt};
                                                                                     # Least Square Error for fit at (c_x,c_y) #
                                                                                                                                                      # \Phi_{LP} #
       return \tan^{-1}(\vec{x}_{opt}[2]/\vec{x}_{opt}[1]);
Given I, N_{\theta}, N_{r}, \theta_{min} = -\pi, \theta_{max} = \pi:
      \vec{\theta}s \leftarrow \text{equispaced grid of } N_{\theta} \text{ points in } (\theta_{min}, \theta_{max});
      w \leftarrow \{ I, \vec{\theta_s}, N_{\theta}, N_r, True \};
      \vec{g}_{geom} \leftarrow 2D min. Search
        (\ C_{csf}(\cdot,\cdot;w),\ (c_{x\ min},c_{x\ max})=(0,\ width(I)),\ (c_{y\ min},c_{y\ max})=(0,\ height(I))\ );
      \Phi_{LP} \leftarrow C_{csf}(\vec{g}_{geom}; I, \vec{\theta}_s, N_{\theta}, N_r, False);
      return (take to (-\pi, \pi) with alg. 1 \{2\Phi_{LP}\})/2
                                                                                                                                 # It returns \Phi_{PL} #
```

#### B.6.9. The Blazquez + RANSAC Cosine Fit Algorithm

It turns out that the cosine square fit algorithm (B.6.8) has many spurious local minima into which it converges, complicating a precise search. Still, we have found that when a good  $\vec{g}_{geom}$  is provided, its estimate for  $\Phi_{LP}$  has a very good precision for lowly noisy images. The Blazquez algorithm (B.6.7) on the other hand, suffers from the converse. The convergence is fast and reliable, with the estimated  $\vec{g}_{geom}$  being very neat, even in noisy scenarios. Yet, its method to extract  $\phi_{CR}$  from  $\vec{g}_{geom}$  is very error-prone. This is because even if  $\vec{g}_{geom}$  is precisely given, the gravicenter is typically displaced from its theoretical position due to the asymmetric noise we find in experimental images. Thus, a natural algorithm arises combining both methods: use the Blazquez algorithm to find  $\vec{g}_{geom}$  and perform a cosine square fit around it to get  $\phi_{LP}$ .

For very noisy crests, the least squares cosine fit still gets very damaged as can be seen in Figure 11: the outliers of the crests will pull the fit out of its place. Consequently an outlier resilient fit method is mandatory for good results. For this, the outlier resilient RANSAC approach (Random Consensus Approach) [41] was adopted (as implemente in the *scikit-learn* Python library [35]). The algorithm followed by RANSAC is explained in the full text.

We can still further generalize the algorithm by allowing the 2D search for  $\vec{g}_{geom}$  to use a weighted mix of the Blazquez cost with the least-square cosine squared fit error (of B.6.8). We could parametrize this cost with a linear parameter  $s \in [0,1]$ , where s=0 would yield the Blazquez algorithm (B.6.7) with the final RANSAC modification, while s=1 would yield the cosine squared fit algorithm (B.6.8) with the RANSAC final distillation. The procedure is summarized in Algorithm 12.

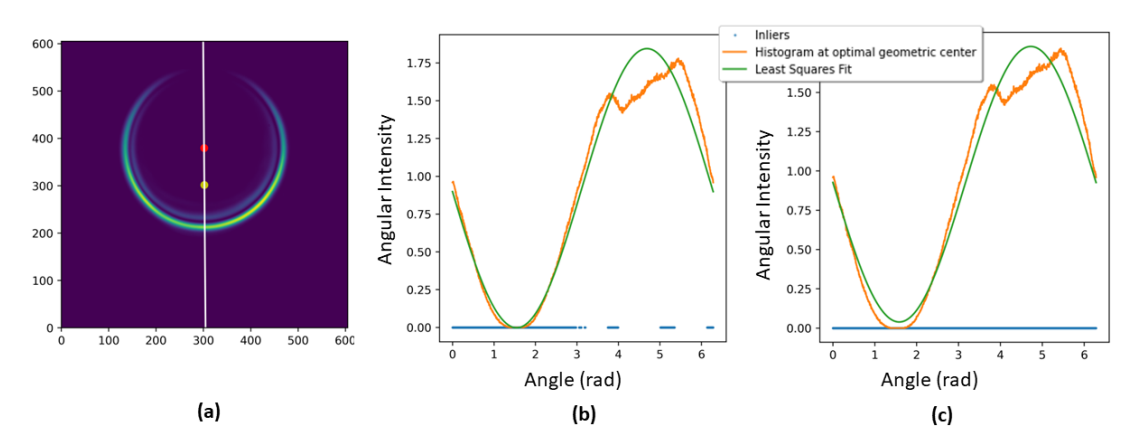


Figure 11: (a) In red, the geometric center found with the Blazquez algorithm. In yellow the gravicenter. The white line indicates the estimated main axis. Using the intensity angular profile of this noisy image around the geometrical center: (a) RANSAC fit of a cosine squared. (c) Least squares fit. Note that in (c), the noisy crests slightly displace the optimal cosine that could be drawn by visual inspection. In (b), we allow to fit the cosine only using the support points in blue (inliers). These were found by RANSAC, which effectively marks the distorted crest as outlier samples.

```
Algorithm 12: The Blazquez + RANSAC Cosine Fit Algorithm - Pseudo-code To get \Delta\Phi_{LP} use I\in\{I_{pb},I_{ref}\}, to get \Phi_{LP},\Phi_{LP} then \Delta\Phi_{LP}=\Phi_{LP}-\Phi_{LP}.
```

```
Def C(\cdot,\cdot; w_{Blz}, w_{csf}, s): # C_{Blz} def. in alg. 10, C_{csf} in alg. 11 # return s \cdot C_{Blz}(\cdot,\cdot; w_{Blz}) + (1-s) \cdot C_{csf}(\cdot,\cdot; w_{csf}) Given I, \vec{g}_{grav}, s, similarity(\cdot,\cdot) N_{\theta}, N_{r}, \theta_{min} = -\pi, \theta_{max} = \pi:

| \vec{\theta}s \leftarrow equispaced grid of N_{\theta} points in (\theta_{min}, \theta_{max}); w_{Blz} \leftarrow \{I, similarity(\cdot, \cdot)\}; w_{scf} \leftarrow \{I, \vec{\theta}s, N_{\theta}, N_{r}, True\}; \vec{g}_{geom} \leftarrow 2D min. Search (C(\cdot,\cdot, w_{Blz}, w_{scf}, s), (c_{x min}, c_{x max}) = (0, width(I)), (c_{y min}, c_{y max}) = (0, height(I)); H \leftarrow matrix with N_{\theta} rows, where k-th row is [1, cos(\vec{\theta}s[k]), sin(\vec{\theta}s[k])]; \vec{x}_{opt} \leftarrow RANSAC solve \vec{x} for linear model \vec{H}\vec{x} \sim \vec{\mathcal{I}} (min_samples, max_trials, resid_thresh); \Phi_{LP} \leftarrow \tan^{-1}(\vec{x}_{opt}[2]/\vec{x}_{opt}[1]); return (take to (-\pi, \pi) with alg. 1 \{2\Phi_{LP}\}/2 # It returns \Phi_{PL} #
```

# B.7. Basic Black-Box Algorithms

An obvious solution to the problem is to train a neural network (NN) to which we input the crescent ring image and we ask it to output the  $\phi_{CR}$  (or the  $\Phi_{LP}$ ) angle. To train it we have practically an infinite number of simulated noisy and non-noisy images of a wide range of possible  $R_0, w_0, z, \phi_{CR}$ .

The most basic idea would be to use a fully connected NN [43] that takes as input the flattened  $605 \times 605$  iX standardized images and outputs  $\phi_{CR}$ . Because the input vector has  $605^2 = 366025$  dimensions, such a NN would need to have many weights to be functional. An option to do this feasible would be to downsample the images before inputting them to the NN. However, we knew the geometrical algorithms (B.6) heavily depended on the resolution of the input images, in a way that the higher their resolution, the predicted results got significantly better. With a similar rationale, on behalf of quantitativeness, we decided not to try this path (it could still be a good option).

Instead, what seemed more reasonable was to let the neural network learn the required down-sampling. This can be done by fitting successive convolutional layers each of which reduce the size of the input data using trainable weights [43]. Only after the size of the data is sufficiently reduced a fully connected NN is plugged in. We implemented two variants. We called one of them Encoder A: it reduces the data until very few dimensions before the fully connected. The second one of them, Encoder B, reduces the data only until an intermediate dimension. Then, a larger fully connected network is plugged in. The architecture of each of the two considered encoders is detailed in Table 1 of the full text. The networks were programmed and trained employing Python's PyTorch library [42], with an Adam optimization algorithm [44] and a decaying learning rate. The input images were iX standardized and divided by their maximum value, to take them to a range [0, 1].

More elaborated and deeper NNs than the suggested ones would possibly give quantitatively better results. However, due to the computational resource limitation, by which a single personal use GPU was available, these were not contemplated as a feasible possibility. In addition, the objective device is to be low-cost, which means the cost of a GPU should only be taken if strictly required.

# B.8. Embedding Space Algorithms

Let us think of the flattened, iX standardized [2X+1, 2X+1] images as vectors  $\vec{v}$  in a  $(2X+1)^2$  dimensional real vector-space. Each of the images is then a point in this  $\mathbb{R}^{(2X+1)^2}$  space. Because when we simulate the crescent ring images we determine them only varying four parameters  $R_0, w_0, z, \phi_{CR}$ , and because all of them cause a continuous change in the image vectors  $\vec{v}$  (we forget for a moment they have a limited bit-depth), this suggests that the set of possible crescent ring images forms a 4 dimensional manifold in  $\mathbb{R}^{(2X+1)^2}$ . We can uniquely label each possible image-vector using four parameters  $R_0, w_0, z, \phi_{CR}$  that if continuously varied cause a continuous variation of the corresponding image-vector  $\vec{v}$ . Thus, we are implicitly defining  $\vec{v}(R_0, w_0, z, \phi_{CR})$ , a parameterization of the hyper-volume in which the possible CR image-vectors lay, employing just four degrees of freedom. This means there should be a transformation  $\vec{\psi}: \mathbb{R}^{(2X+1)^2} \to \mathbb{R}^4$  that takes the points in  $\mathbb{R}^{(2X+1)^2}$  and embeds them in  $\mathbb{R}^4$  in a way that every different image-vector  $\vec{v}$  goes to a different  $\mathbb{R}^4$  point. If the transformation function  $\vec{\psi}$  is fast enough, then, this could be a useful representation space for the images, since a classification or regression task could be simpler in a smaller dimensional space. Moreover, we could design the embedder  $\vec{\psi}$  to place the samples in a configuration that is more convenient for the labeling of non-labeled samples that we embed between already labeled samples.

# B.8.1. Identifying the Dimensionality of the Data Manifold

Assuming all data lays in such a four dimensional manifold is a bit restrictive and unrealistic. This is mainly because experimental images will always have noise. For each of the possible degrees of freedom in which each noise source can be parameterized, we will be introducing a possibly new degree of freedom in the data manifold (most noise sources generate images that were not among the

theoretically perfect  $R_0, w_0, z, \phi_{CR}$  crescent rings, so a new curvilinear direction in  $\mathbb{R}^{(2X+1)^2}$  will be explored). For example, if we considered the artificial noise we described in (B.2) to be a faithful representation of noise (which is clearly not), then, the number of Gaussian blobs in each image, their location and standard deviations, their strength etc. would also implicitly be involved in the parametric definition of  $\vec{v}$ . This could lead us to conclude that because there could be an unlimited number of noise factors, experimental data is not in a low dimensional manifold anymore. And that might be true, but even still, it might be useful to choose a low dimensional embedding space representation, because (a), it could be enough for the quantitativeness we seek, or more importantly (b), it could be forced to take the noisy images and send them to the same low dimensional neighborhood, implicitly acting as a de-noiser. That is, a lower dimensional representation could end up "correcting" the data manifold that started to "slip through our fingers" when we began to introduce noise degrees of freedom, and could mould it back to the (ideally 4) lower dimensional manifold. Whether this is possible or not would be determined by whether it is technically possible to tell which is the original "ground-truth" that formed a given noisy image. That is, whether each noisy image can really be uniquely traced back to its Platonic crescent ring: whether the stochastic noise function is injective in a sense. This seems to be an unfair assumption, but could work for many noise sources. Thus, possibly there is a reasonable lower dimensional embedding space where we can fit the data, but this will need to have more than 4 dimensions to allow the accommodation of these "degeneracies".

The question is then: which one is a "reasonable dimension"? For this, we could design embedding functions  $\vec{\psi}$  for several dimensions and evaluate how well they preserve the structure of the original dataset. This is what is called in general a "reconstruction error" [45], and we will call the *preservation error*. As we keep lowering the dimensionality of the embedding space, the preservation error will clearly keep increasing (for there will be subtle degrees of freedom that will inevitably be lost). Yet, a serious steep increase is expected to appear when we drop the dimension below a certain threhsold, in which many far away samples start to be sent to colliding embeddings. We could geometrically imagine this point as the dimension in which the data manifold no longer "comfortably fits in". Then, this will indicate the effective dimensionality of the data manifold.

To perform this test, we have chosen algorithms that look for embedding functions  $\vec{\psi}$  trying to preserve several aspects of the structure of the manifold. These are: the Multidimensional Scaling (MDS) [47], which tries to preserve inter-point distances, the Uniform Manifold Approximation and Projection (UMAP) [50], which tries to preserve the topological structure of the manifold, and the NCA algorithm [51], trying to preserve the ability to predict the label of a sample by its proximity to the adjacent points (in a sense trying to preserve the continuity caused by having an equal label).

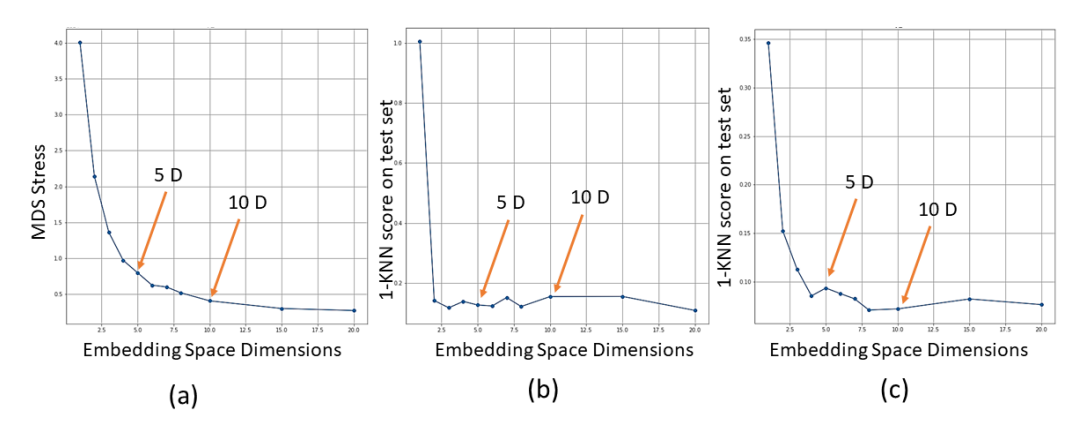


Figure 12: (a) MDS stress as a function of the embedding space dimension. (b) 1-KNN Regression score (k = 5) by UMAP embedder as a function of embedding space dimension. (c) 1-KNN Regression score (k = 5) by NCA embedder as a function of embedding space dimension.

We can see in Figure 12, the preservation errors found by the MDS, UMAP and NCA methods as a function of the embedding space dimension of the obtained embedders (employing 2000 samples from the noisy image dataset to train them). As reconstruction error for MDS, the stress function characterizing it was chosen, while for NCA and UMAP, a k=5 nearest neighbour regression score

was employed for a test set of 500 labeled samples transformed by the trained embedders. We can see that the optimal effective dimensionality of the embedding space could be fixed, in accordance with the three methods, around 10 dimensions. From here on, this dimensionality will be assumed for all the embedding space algorithms of the work.

# B.8.2. Metric Learning and Nearest Neighbors

The potential purposes for embedding functions  $\vec{\psi}$  in this work are twofold:

- (a) On the one hand, the distance between the images in the embedding space can be used as a similarity metric (to be used in the geometric algorithms (B.6) or the simulation fit algorithms (B.9)). The reason why they could be useful instead of using directly an Euclidean distance metric or the MAE (18) for the un-embedded images, is that some embedding algorithms are trained to evade noise, or to preserve only the most significant variability axes of the data manifold. This can turn out to work as an implicit de-noiser.
- (b) On the other hand, embedding spaces are usually trained to agglomerate data samples with the same or similar labels. Thus, they are the perfect scenario to apply a K-Nearest Neighbour (KNN) Regression, which essentially works as follows. Given an unlabeled sample  $\vec{v}_{N+1}$ , we embed it as  $\vec{\psi}(\vec{v}_{N+1})$  and we look for the K closest embedded samples for which we have a label. Then, we predict the label of  $\vec{v}_{N+1}$  as the average label of the neighbors, weighted by their distances to the sample. We know that in the original space, the images already varied continuously with the label  $\phi_{CR}$ , so we could already expect a KNN to work there. If then the embedders are trained to increase the proximity between common labels, the effectiveness of KNN should only increase. In our implementation, we will be using the Ball Tree [46] variant of the KNN algorithm to deal with higher dimensional and more numerous datasets, with a k=3, as implemented in scikit-learn [35]. See the procedure followed to get  $\Phi_{LP}$  in Algorithm 13.

A remaining question is whether we should employ the noisy or the non-noisy dataset to train the embedders and the KNN. For metric learning as well as the KNN, it seems that the noisy dataset should be preferred, for their aim is to include the effect of realistic data (which is noisy). However, for the embedder learning the answer is not that clear. Because noisy data can act as bridges between portions of the manifold that otherwise should not be directly connected, it could happen that the fine local structure of the manifold is spoiled by training them with noisy data. Also, it could happen that if instead we train them with non-noisy data, the embedder acts as a natural denoiser, taking the samples that lay outside the core manifold to "their place". However, it might happen, as we discussed previously, that there are noisy images that could have been generated by different  $\phi_{CR}$ . A degree of freedom to represent them can only be captured if we use noisy images in the training. Therefore, we will try both approaches and see what is the best one in each case.

```
Algorithm 13: Embedding Space KNN Regression - High Level Pseudo-Code To get \Delta\Phi_{LP} use I\in\{I_{pb},I_{ref}\}, to get \phi_{CR}, \phi_{CR} then \Delta\Phi_{LP}=(\phi_{CR}-\phi_{CR})/2.
```

```
Given I, \ \vec{\psi}, \ embedded\_dataset, \ K:
I \leftarrow (\ \text{iX standardize}\ (I)\ )/max(I);
I_e \leftarrow \vec{\psi}(I);
closest\_labels, \ closest\_dists \leftarrow \text{get label}\ (\phi_{CR}) \text{ and distance to } K \text{ closest}\ \vec{\psi}(\text{samples}) \text{ in dataset}
(I_e, \ embedded\_dataset, \ K);
\phi_{CR} \leftarrow \text{average label weighted by inverse distance}\ (closest\_labels, \ closest\_dists);
\mathbf{return}\ (\text{take to}\ (-\pi,\pi) \text{ with alg. 1}\ \{\phi_{CR}\})
# It \mathbf{returns}\ \phi_{CR}#
```

#### B.8.3. Employed Algorithms to Generate Low Dimensional Embedders

We offer in what follows the list of the employed embedding generation algorithms, together with a visual representation of the embedding spaces generated in each case (for which a PCA is applied

on the embedded training samples). This section in the full dissertation contains a deeper and more detailed description of each algorithm.

The CNN Triplet Loss embedder was implemented using the *Pytorch* library [42] and the custom architecture in Table 1 of the full text. MDS, PCA, KPCA, Isomap and LLE were used through their implementation in the *scikit-learn* library in Python [35]. For UMAP, the implementation offered as the *umap-learn* [49] Python library was employed.

- (Metric) Multi-dimensional Scaling (MDS): Given a fixed embedding space dimension n and a representative sub-set of the observable samples  $\{\vec{v}_k\}_{k=1}^N$  with  $\vec{v}_k \in \mathbb{R}^{(2X+1)^2}$  (flattened crescent ring images of varying  $R_0, w_0, z, \phi_{CR}$ ), MDS [47] looks for a set of corresponding positions  $\{\vec{e}_k\}_{k=1}^N$  with  $\vec{e}_k \in \mathbb{R}^n$ ,  $n < (2X+1)^2$ , such that the distances between the samples in the original space  $d(\vec{v}_j, \vec{v}_k)$  are equal to the distances between the corresponding points in  $\mathbb{R}^n$ ,  $d(\vec{e}_j, \vec{e}_k)$ ; with  $d(\cdot, \cdot)$  a fixed distance metric.
- Uniform Manifold Approximation and Projection (UMAP): This is a manifold learning method that unlike many others, has a heavy mathematical machinery backing its consistency, as the original references show [50, 49]. Qualitatively, the main thing this machinery proves is that the manifold from which the observed set of points  $\{\vec{v}\}_{k=1}^N$  is sampled, can faithfully be represented by a simplicial complex which at the same time, thanks to the Vietoris-Rips construction, can reasonably be described by only using 0- and 1-simplices (points and lines) generating a graph. The main result backing this correspondence comes from the so called "Nerve theorem" [50], by which the simplicial complex is homotopically equivalent to the manifold. Then, the key idea is that if the same complex is replicated in a lower dimensional space, we can have certainty that the complex represents a topologically equivalent manifold in lower dimensions.
- Neighborhood Component Analysis (NCA): The essential idea of NCA [51] is to find a linear application A (represented by an  $n \times (2X+1)^2$  matrix) taking the image-vectors in  $\mathbb{R}^{(2X+1)^2}$  to  $\mathbb{R}^n$ , in a way that the closest points in the embedding space have common labels.
- Principal Component Analysis (PCA): This is a well known classical method [53]. Essentially it finds the directions in the space of features (in our case the pixels), along which the data presents maximum variance, using the diagonal decomposition of its covariance matrix. Then, by assuming that what gives discriminative power is having a bigger variability in the describing features of a sample, it just leaves the n most informative linear combinations of the features. Because it does not employ the labels to generate the embedder, it possibly destroys part of the information that was relevant for label prediction. Yet, it is true that the chosen axes could turn out to represent the  $R_0, w_0, z, \phi_{CR}$  degrees of freedom, for they are for sure implicated in the biggest of the variations in the resulting image intensity values. Thus, it could happen that the information "it destroys" is precisely the jitter introduced by noise.
- Kernel PCA: This technique [54], implicitly embeds first the data into a higher dimensionality space than the data feature dimensions  $(2X + 1)^2$ , to then take its first  $n < (2X + 1)^2$  principal components (using PCA). The rationale of doing this is that even if in the original feature space differently labeled samples could not be separated by means of simple boundaries (like hyperplanes), if we throw them into a higher dimension, we could arrange them to be easily separable. Then, by only taking the n most informative directions of this high dimensional space we may still be able to separate the labels easily, now in a lower dimension.
- **Isomap**: This is a version of MDS that allows a better preservation of the manifold's local connectivity [48], by using as distance metric the geodesic distance between the points restricted to a neighborhood graph similar to the one employed by UMAP.
- Locally Linear Embedding (LLE): The LLE method [52], just as Isomap, looks to preserve the local structure of the manifold; this time trying to express each point with the same linear combinations of its neighbours in the original space.

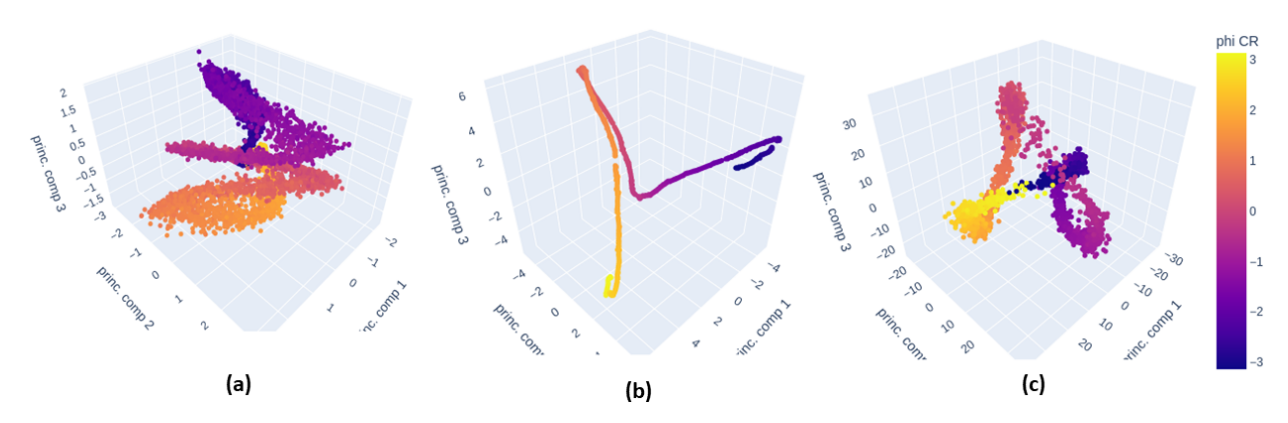


Figure 13: Samples of the noisy dataset embedded using the trained embedders to 10D, and reduced dimensionally using PCA to 3D for visualization. (a) PCA, (b) UMAP, (c) NCA.

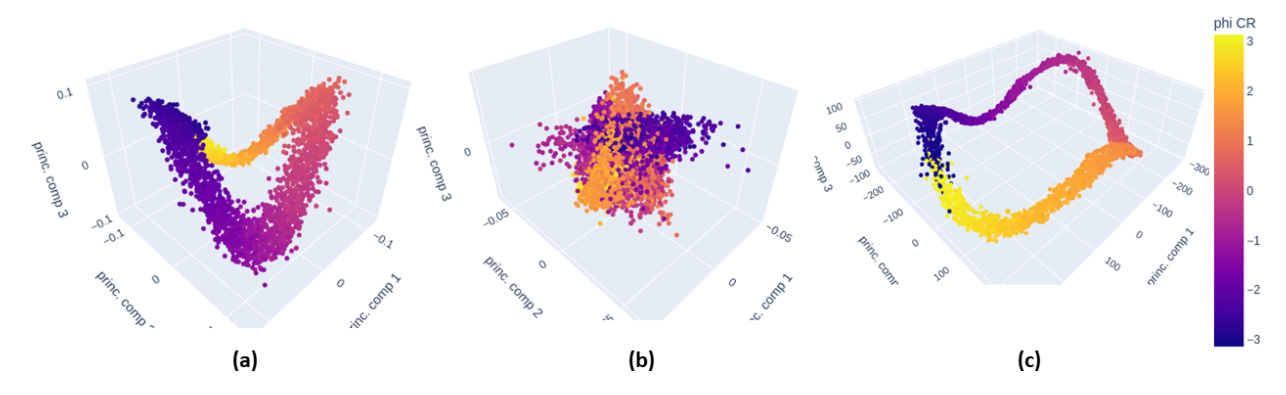


Figure 14: Samples of the noisy dataset embedded using the trained embedders to 10D, and reduced dimensionally using PCA to 3D for visualization. (a) KPCA, (b) LLE, (c) Isomap.

• Triplet Loss Convolutional Neural Network Embedder: Both to be used as a preprocessing function to run a KNN regression or to be used as a similarity metric, the most ideal of the embedders  $\vec{\psi}_{\vec{w}}: \mathbb{R}^{(2X+1)^2} \to \mathbb{R}^n$  should metrically separate as much as possible semantically different samples (with different  $\phi_{CR}$  label) and make as metrically close as possible semantically similar samples (with similar  $\phi_{CR}$ ). We can try to obtain such an embedder by training the parameters  $\vec{w}$  of a parametrized emebdding function  $\vec{\psi}_{\vec{w}}$ , like a NN, with an objective cost function following the stated idea. These kind of cost functions are named as Triplet Losses. Following [55], a feasible implementation to be used in our datasets, where we have almost infinite samples and thus we will perform a batched training, would be to partition the dataset in PK sample batches. P different images  $\vec{v}_j^{\phi_{CR_j}} \in \mathbb{R}^{(2X+1)^2}$  of different  $\phi_{CR_j} \in (-\pi, \pi]$  are randomly chosen in each batch, and for each of them K random noisy versions  $\vec{v}_k^{\phi_{CR_j}}$  with the same label  $\phi_{CR_j}$  are sampled. The employed cost function and NN architecture, together with a small view of some training metrics and the embedded space, can be found in the full text.

# **B.9. Simulation Fitting Algorithms**

Because we can simulate the crescent rings that should appear in the experimental images if all the theoretical considerations were in order, an obvious algorithm to try is to fit theoretical images to the desired experimental ones until we find a perfect match. That is, not only could we estimate  $\phi_{CR}$  and thus  $\Phi_{LP}$ , but also all the other theoretical degrees of freedom  $R_0, w_0, z$ . For this, we can perform a 4D multidimensional optimization to look for the simulated image that is most similar to the experimental one. This algorithm is slower than the rest of the suggested ones, because the simulation of each theoretical image in the optimization takes a considerable time. We can fasten it, by considering the D matrix trick explained in (B.3), yet, it will still not be the fastest algorithm.

In principle, the equations in (A.3) generate crescent ring images centered in the geometrical

centers. For the experimental images on the other hand, in principle we only know their gravicenter. Thus, the immediate algorithm to compare a simulated image with an experimental one would be to first center the simulation as well in its gravicenter (through the iX standard), then, to apply a common pre-processing to take both images to the same intensity ranges. We implemented this method following Algorithm 14, by using the Mother Dataset of (B.3) as the simulated image grid.

Algorithm 14: The Simulation Fit Algorithm (Gravicenter) - High Level Pseudo-Code To get  $\Delta\Phi_{LP}$  use  $I \in \{I_{pb}, I_{ref}\}$ , to get  $\phi_{CR}$ ,  $\phi_{CR}$  then  $\Delta\Phi_{LP} = (\phi_{CR} - \phi_{CR})/2$ . **Def**  $C_{sim}(R_0, w_0, z, \phi_{CR}; I, mother\_dataset, similarity(\cdot, \cdot), pre\_process(\cdot))$ : # Dataset contains [2,2] D matrices per  $[H_{simul},W_{simul}]$  pixel as explained in B.4.  $D \leftarrow \text{get closest } (R_0, w_0, z) \text{ D matrix in } mother\_dataset$  # Array of shape  $[2, 2, H_{simul}, W_{simul}]$  #  $D\_vectors \leftarrow \text{matrix dot vector } (D, [cos(\phi_{CR}), sin(\phi_{CR})])$ # Shape  $[2, H_{simul}, W_{simul}]$  # # Remember  $I(x,y) = |\vec{D}(x,y)|^2$  #  $I_{simul} \leftarrow \text{complex Euclidean norm } (D\_vectors)$  $I_{simul} \leftarrow \text{pre-process}(I_{simul})$ **return** -similarity  $(I_{simul}, I)$ **Given** I,  $mother\_dataset$ ,  $similarity(\cdot, \cdot)$ ,  $pre\_process(\cdot)$ ,  $(R_{0min}, R_{0max}), (w_{0min}, w_{0max}), (z_{min}, z_{max}), (\phi_{CRmin}, \phi_{CRmax}):$  $I \leftarrow iX \text{ standardize ( pre_process}(I) );$  $w \leftarrow \{I, mother\_dataset, similarity(\cdot, \cdot), iX\_standardize(pre\_process(\cdot))\};$  $R_0, w_0, z, \phi_{CR} \leftarrow 4D$  min. Search  $(\ C_{sim}(\cdot,\cdot,\cdot,\cdot;w),(R_{0min},R_{0max}),\ (w_{0min},w_{0max}),\ (z_{min},z_{max}),\ (\phi_{CRmin},\ \phi_{CRmax})\ );$ **return** (take to  $(-\pi, \pi)$  with alg. 1  $\{\phi_{CR}\}$ )

An alternative version was implemented following Algorithm 15. It uses the fact that the Blazquez algorithm (B.6.7) is very good at finding the geometric center of noisy images, with a precision presumably better than the precision with which we estimate the gravicenter. Then, it is the experimental images that are centered in the geometric centers, before comparing with the simulations, which are centered likewise by default.

```
Algorithm 15: The Simulation Fit Algorithm (Geometric Center) - Pseudo-Code To get \Delta\Phi_{LP} use I\in\{I_{pb},I_{ref}\}, to get \phi_{CR}, \phi_{CR} then \Delta\Phi_{LP}=(\phi_{CR}-\phi_{CR})/2.

Given I, mother\_dataset, similarity(\cdot,\cdot), pre\_process(\cdot), C_{Blz} of alg.10, C_{sim} of alg.14, (R_{0min},R_{0max}), (w_{0min},w_{0max}), (z_{min},z_{max}), (\phi_{CRmin},\phi_{CRmax}):

I\leftarrow iX standardize (pre\_process(I));
w\leftarrow\{I,similarity(\cdot,\cdot)\};
\vec{g}_{geom}\leftarrow 2D min. Search
(C_{Blz}(\cdot,\cdot;w),(c_{x\,min},c_{x\,max})=(0,\,width(I)),(c_{y\,min},c_{y\,max})=(0,\,height(I)));
I_{geom}\leftarrow iX standard but using alternative center (I,\,\vec{g}_{geom})
w\leftarrow\{I_{geom},\,mother\_dataset,\,similarity(\cdot,\cdot),\,pre\_process(\cdot)\};
R_0,w_0,z,\phi_{CR}\leftarrow 4D min. Search
(C_{sim}(\cdot,\cdot,\cdot,\cdot;w),(R_{0min},R_{0max}),\,(w_{0min},w_{0max}),\,(z_{min},z_{max}),\,(\phi_{CRmin},\,\phi_{CRmax}));
return (take to (-\pi,\pi) with alg. 1 \{\phi_{CR}\})

# It returns \phi_{CR} #
```

# B.10. Pipeline to Compare the Algorithms and Preprocessings

For each algorithm we have several possible variants, since we have several pre-processing functions, several optimization methods, several embedders etc. In order to estimate the performance of all of them and find the best configurations and best overall algorithms, we run a pipeline of tests employing both the noisy simulated image dataset and non-noisy image dataset, annotating the absolute errors in the prediction of  $\Delta\Phi_{LP}$  and the times taken to get these results. The non-noisy dataset will test the precision and timing of the algorithms in the best of the cases, for all the range of acceptable  $R_0, w_0, z$  crescent rings, **conditioned on the resolution of the camera being**  $540 \times 540$ . The noisy dataset on the other hand, will test the robustness of the algorithms against very noisy conditions (considerably noisier than the experimentally found ones), for all the range of acceptable  $R_0, w_0, z$  crescent rings (the "worst case-scenario"); again assuming the camera resolution is the fixed one.

#### B.10.1. Results on the Simulated Datasets

All the carried tests and their results, gathered algorithm-wise and image-wise can be found in the /RESULTS folder in the Github repository of the project [23]. In Tables 2 and 1 we gather only the results of the best found configuration of each algorithm (best combination of pre-processing, embedding function, hyperparameters etc.) for the noisy and non-noisy simulated image datasets respectively. We consider the best variant of an algorithm to be the one providing the lowest upper bound of the confidence interval for the expected absolute error.

**Table 1:** Summary of the best variant found for each algorithm on 1000 random samples of the **Non-Noisy** Image Dataset. CI stands for the bootstrap-t confidence intervals [56] for the expectation. Ordered by increasing mean absolute.

Algorithm		Absolute Error (rad)			Times (s)	
Name	Winner Variant	Mean	90% CI		% CI   90% CI	
Mirror Flip	Quadratic Opt., Lanczos Interpol., Preproc. Norm. to Max	0.00106	0.00102	0.00109	0.218	0.220
Gravicenter Regression	Preproc. Norm. to Max	0.00196	0.00189	0.00203	0.453	0.454
Kalkandjiev-Rotation	Quadratic Opt., Lanczos Interpol., Preproc. Norm. to Max	0.00205	0.00198	0.00213	0.221	0.222
Blazquez + Cosine Fit	w=0.999, Nelder-Mead Opt., Preproc. Norm. to Max	0.00455	0.00437	0.00475	3.38	3.39
Cosine Square Fit	Preproc. Norm. to Max	0.00466	0.00452	0.00480	2.820	2.830
Blazquez	Preproc. Norm. to Max	0.124	0.0517	0.274	0.454	0.456
Simulation Fit	Opt. Nelder-Mead, About Grav. Preproc. Norm. to Max	0.140	0.123	0.171	1.283	1.316
KNN+Embedder	NCA Embedder, Trained with Non-Noisy Data	0.280	0.140	2.32	0.130	0.160
KNN	Trained with Non-Noisy Data	0.820	0.484	1.40	4.960	5.610
Bimodal Histogram	Preproc. Norm. to Max	1.66	1.58	1.76	0.131	0.132
Relative Rotation	Quadratic Opt., Bicubic Interpol., Preproc. Norm. to Max	1.73	1.61	1.83	0.068	0.069
Polar Registration	Preproc. Norm. to Max	2.83	2.64	3.04	0.245	0.245
CNN+fc	Encoder A	3.41	2.94	4.06	1.093	1.094

We find that for the given camera resolution, in the best-case-scenario, the Mirror Flip algorithm is the best algorithm, allowing the determination of the linear polarization angle with a precision of  $\pm 0.001$  deg. Note that if we performed the same study with a bigger resolution, the results would be orders of magnitude better, as preliminary checks have shown us. The exact dependence and the asymptotic limit will be studied in a future work. The Mirror Flip algorithm in addition, is capable of determining the angle within a fifth of a second. This speed would be slightly reduced by higher resolution images. Yet, the current implementation in Python is not thought to be the fastest one. Ad hoc optimization, writing the algorithms in a lower level language like C, would make them faster.

On the other hand, the results on the noisy image dataset show that the robustest algorithms in front of noise are the Simulation Fit and the Kalkandjiev-Rotation, closely followed by the Mirror Flip algorithm. The first one offers the smallest mean absolute error of  $\pm 1.86$  deg, compared with the  $\pm 1.93$  deg of the second one, but taking more time (1.24 s against 0.22 s). This time difference can be very significant, because for real-time measurements it is desirable to have more than one measurement per second.

Some additional points must be noted on the results. On the one hand, we see that the deep learning approaches have performed very poorly: the convolutional encoders are the worst algorithms and the Triplet Loss embedder is neither the best embedder for KNN, nor the best metric for the Simulation Fit. This is possibly due to the limited training of the networks and to the fact that we could not try different hyperparamter and architecture combinations. Also, it could be that networks built from scratch need better losses or way more time of training to achieve quantitative results as the ones we require. Trying a transfer learning from pre-trained networks on more difficult computer vision problems, is something left as future work.

Apparently, using the mixed Blazquez and cosine squared fit cost is better than using only either of them, even when we allow them both to have the last guess of the angle done with a RANSAC cosine squared fit.

**Table 2:** Summary of the best variant found for each algorithm on 1000 random samples of the **Noisy** Image Dataset. CI stands for the bootstrap-t confidence intervals [56] for the expectation. Ordered by increasing mean absolute.

Algorithm		Absolute Error (rad)			Times (s)	
Name	Winner Variant	Mean	90% CI		90% CI	
Simulation Fit	Opt. Powell, About Gravicenter, Preproc. Sigmoid k=35 c=0.1	1.86	1.75	1.98	1.24	1.25
Kalkandjiev-Rotation	Opt. Fibo., Bicubic Interpol., Preproc. Sigmoid k=35, c=0.1	1.93	1.85	2.01	0.218	0.219
Mirror Flip	Opt. Quad., Lanczos Interpol., Preproc. Sigmoid k=35, c=0.1	2.01	1.92	2.12	0.220	0.222
Simulation Fit + Embedder	Opt. Nelder-Mead, About Gravicenter, Preproc. NCA trained w. Noisy Data	2.02	1.88	2.21	2.68	2.73
Blazquez + Cosine Fit	w=0.9999, Opt. Nelder-Mead	2.29	2.18	2.40	3.46	3.47
Blazquez	Opt. Nelder-Mead, final estimation using RANSAC+cos fit	2.32	2.20	2.46	0.510	0.512
KNN + Embedder	Embedder NCA, Trained w. Non-Noisy Data	2.32	2.01	2.94	0.04	0.05
Cosine Square Fit	Opt. Nelder-Mead	2.83	2.73	2.93	2.865	2.866
Gravicenter Regression	Preproc. Sigmoid k=35 c=0.1	2.88	2.77	2.98	0.45	0.45
Polar Registration	Preproc. Sigmoid k=35 c=0.3	2.88	2.74	3.10	0.246	0.247
Relative Rotation	Opt. Quad., Bicubic Interpol., Preproc. Opening s=11	2.94	2.82	3.06	0.067	0.068
Bimodal Histogram	Preproc. Sigmoid k=35, c=0.1	3.41	3.28	3.54	0.131	0.132
KNN	Trained w. Non-Noisy Data	3.69	3.19	4.46	0.886	0.893
CNN+fc	Encoder A	4.09	3.69	4.65	1.092	1.093

An interesting observation, if one looks at the full results in the Github [23], is that for all the different embedders, the best results on the noisy dataset were given when the embedders were trained with non-noisy data; except for the UMAP algorithm, which apparently achieved a correct characterization of the noisy data manifold. For the rest of embedders, this could be because they indeed act as de-noising functions implicitly, following our discussion in (B.8).

Finally, regarding the ordering in the ranking for the non-noisy and noisy datasets, we see that some of the algorithms that perform very well in the abscense of noise, like the Gravicenter Regression, which is the second best one, get very damaged by noise, arriving to be one of the worst algorithms in the presence of heavy noise. The same happens for the Cosine Square Fit for example. Yet, others like the Mirror, Kalkandjiev Rotation or the Blazquez+Cosine Squared Fit (with RANSAC), seem to be affected in a similar weight by noise, since they preserve their order in the ranking. The robustest one however appears to be the Simulation Fit algorithm, because it gets to be the first one in the ranking with noise, while it is not the first one in the non-noisy scenario.

# Part C: The Body of the Polarimeter

In this part, we will review how CR rings can be experimentally generated and measured, and we will design with it the hardware for the device, following the suggested one in Ref. [13]. We will then analyze the experimental images of the CR rings we obtain, noting their noise sources. With them we will test the designed algorithms. Finally, we will sketch the proof-of-concept device, analyze its cost and whether there could be any place for it in the market.

# C.1. Experimental Setup to Observe Conical Refraction Rings

The standard way to observe the CR phenomenon, following the theoretical considerations in Part A and Refs. [11, 10] (such that we want to compare the results with the simulations of the BKB theory), is to set-up the following elements in an optical track:

- (a) Set-up a **light** source that generates a collimated coherent beam with a well defined wavelength (monochromatic) and a cylindrically symmetric transversal profile. The beam should be thin enough to avoid significant interference with the walls of the biaxial crystal. It should preserve its coherence until its arrival in the camera sensor. In addition, since we want to compare it with the predictions of the BKB theory, it should have an adequate transversal profile to satisfy the paraxial approximation, and should have approximately the same polarization state everywhere in a given transversal section. In particular, it is very convenient for the simulation comparison if it has a Gaussian transversal intensity profile.
- (b) First of all, the beam is passed through a **linear polarizer**, which will make sure the wave will be describable using a Jones vector  $\hat{u}_J = (cos(\Phi_{LP}), sin(\Phi_{LP}))$ , following the notation of part A, for a certain  $\Phi_{LP} \in (-\pi/2, \pi/2]$ .
- (c) At this point a  $\lambda/4$  wave-plate can be placed to generate CP and ease the alignment of the crystal. Otherwise it is here where we place the problem **sample** that rotates the LP plane.
- (d) Next, the beam is focused by a **convergent lens**, so that the sharpest CR rings are generated at a finite distance, in the focal plane.
- (f) The focused beam is made to enter and leave the **biaxial crystal** before it arrives to the focal plane. It is important that the light beam exactly hits the crystal at an orthogonal angle with its face, which at the same time must be orthogonally cut with respect to one of its optical axes.
- (g) At the focal plane (which will be a bit farther than the naively expected plane, due to the passage through the crystal), we can place a **camera** to see the generated z = 0 parameter CR ring (following part A).
- (h) For the algorithms we described in Part B, and for inspection in general, it is more convenient to have a physically bigger ring, so that it covers more pixels of the camera's sensor. To achieve this, an option could be to make the crystal longer, since the geometric radious of the ring fulfills  $R_0 = \alpha L$ , where L was the length of the crystal, as we saw. However, a more convenient trick is to magnify the image of the focal plane employing a second convergent lens at its focal distance from z. The magnification factor will be proportional to the ratio of their focal lengths.

#### C.1.1. The Test Set-up

The set-up we employed to take the experimental images for great part of the study can be seen in Figure 15. In this set-up, we generated the light beam (a) with the LED diode array model M590F3 3.3 mW, provided by Thorlabs, which generates monochromatic light of 590 nm. This LED array is

inside a case that conducts its light out through a fiber. The light is then inputed to a single-mode fiber that only allows the Gaussian transversal mode of the beam to propagate through. At the output, a collimator is employed to collimate the Gaussian beam.

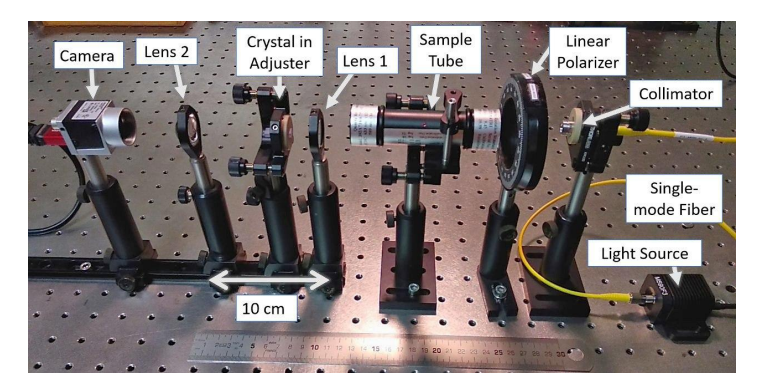


Figure 15: Experimental set-up with the LED M590F3 light source, explained in the text.

In an alternative set-up, we replaced the light source by an He-Ne laser of 632.8 nm (model Uniphase 1135P, 10 mW), which directly generates a Gaussian profile beam. We placed a light attenuator in its output to reduce its power before it entered to the rest of the set-up.

The employed crystal for all the work was a monoclinic centrosymmetric  $KGd(WO_4)_2$  rectangular prism of sizes  $6 \times 4 \times 20mm$ , with its small faces cut orthogonally to one of the optical axes.

Two different lens settings, causing two different  $\rho_0$  were employed. For the LED beam, a first lens (after the light source) of 25 mm focal length and a second lens (for the magnification) of 50 mm were used. For the He-Ne laser, the focal length was 50 mm for the first lens, while 200 mm for the second one.

The employed camera in all experiments was a Basler acA720-520um with a global shutter CMOS sensor of  $720 \times 540$  pixels of resolution (6.9 $\mu m$  side square pixels).

#### C.1.2. Calibration of the Set-up

The most subtle thing to achieve a correct CR ring is to correctly align the light beam with the biaxial crystal. For this we employ a holder for the crystal with two micrometric screws (as can be seen in Figure 15) that allow us to adjust it in spherical coordinates. This calibration was typically done by visual inspection. The typical approach was to set a  $\lambda/4$  wave-plate after the first linear polarizer, in the slot (c), with a  $\pi/4$  rad inclination of its main axis relative to the LP of light. This generates a CP light, that should generate a hollow ring in the camera's plane, as we saw in Part A. If the beam is not properly aligned, instead, a sequence of ellipsoids that split up until only two points are visible due to birefringence (when the beam gets very misaligned) can be seen in the camera (see example images in Figure 2.3. of Ref. [10]).

In order to help the manual procedure, three real time image processing methods were designed. The implementation scripts can be found in the project Github [23], with the rest of generated code.

Method 1. Analyze the Uniformity of the CP Hollow Ring: By setting a CP input light, we can pass the images of the camera in real time from Blazquez's Algorithm (B.6.7) to obtain their geometrical centers. Then, by equation (11), we know that the angular profile around this center should be a constant when the light beam goes exactly along the optical axis. We fit a line to the angular profile and print in real time the slope of the fitted line. The optimal crystal-beam configuration will be achieved when the slope is closest to zero and visually the ring satisfies the proper intuition. There will always be experimental noise, meaning we will never obtain a flat angular profile. Thus, the RANSAC method [41] is used to fit the line (instead of a least squares approach), since it allows us to get rid of the outliers that unbalance the line.

Method 2. Analyze the proximity of the Image to a Simulated Image: We are able to simulate the perfect theoretical rings that should appear in the camera when the input light beam exactly goes along the optical axis. Then, in real time we can apply the Simulation Fit algorithm of section (B.9) to the captured images, and plot not only the found closest theoretical image to the experimental one, but a similarity metric, like the mean square error between the two images. We can do this both for input LP and CP. Then, we adjust the crystal until the fitted theoretical image has the least possible mean square error.

Method 3. Analyze the Proximity of the angular profile to a Squared Cosine: From equation (14) we know that for input LP, when the light beam goes along the optical axis, the intensity profile about the geometrical center should be a cosine squared. Then, by setting an input LP, we apply in real time the Blazquez+RANSAC cosine fit algorithm of section (B.6.9), which will show us the angular intensity profile along the geometrical center of the ring, together with the best RANSAC cosine square fit. We adjust the crystal until the generated profile has a minimum fit error.

The procedure could be improved even more if we had an electronic component to control the crystal adjustment with a computer. If so, we would simply apply a 2D optimization algorithm like the ones described in part B, on the degrees of freedom moving the crystal.

# C.2. Non-Idealities in the Experimental Rings

As can be seen in Figure 16, experimental images, even the ones taken with care to build the test datasets, present notable noise, breaking the theoretical assumptions not only about the background, but especially about the predictable intensity profile of the rings. We can see in these images that essentially not even a single symmetry of those listed in (B.1) is fulfilled. Yet, we expected the quality and robustness of the algorithms to be enough to render the effect of noise at least for an interesting resolution, which turned out to be the case.

Let us list the main noise sources we encountered and how we managed to partially solve them:

- Each camera pixel sensor, in the end, is counting the number of light energy packages (so called photons) that arrive to it. These arrivals happen randomly, but ideally, each pixel should detect an expected number of photons per unit time, proportional to the intensity of the electric field. These are essentially the assumptions of the Poisson model, as derived in Ref. [59]. The random variable for the photon count in each pixel  $V_{x,y}$  then follows a Poisson distribution  $V_{x,y} \sim Poiss(\lambda = \alpha I(x,y))$ , with I(x,y) the deterministic pattern without this count-noise and  $\alpha > 0$ . Such a noise can be diminished by averaging over N images  $I_k \sim V_{x,y}^{(k)}$ . This is because without changing the experiment, images are independent random samples of the identically distributed  $V_{x,y}^{(k)}$ . Then  $I_{average} = \sum_k V^{(k)}/N$ , meaning the variance on each pixel is reduced by a factor N:  $var_{x,y}[I_{average}] = \sum_k var[V_{(x,y)}^{(k)}]/N$ , where  $var[V_{(x,y)}^{(k)}]$  is constant, while the expectation is still the same  $E[I_{average}] = E[V_{x,y}^{(k)}] = I(x,y)$ . Thus we get an improved signal to noise ratio. Note that for the interpretation as photon counts, averaging is equivalent to increasing the exposition while avoiding the pixel saturation, which is an alternative solution.
- If the optical fiber from which the laser is outputted allows the passage of other modes than the Gaussian one, the shape of the generated rings need not be equal to the ones we solved in (A.3). This can be easily solved with a single-mode fiber for the particular wavelength, that due to physical constraints avoids the passage of higher order Laguerre-Gaussian modes that solve the paraxial Helmholtz equation in cylidrically symmetric coordinates. Alternatively, employing other techniques to light the crystal, that lead to similar rings (like placing a pinhole after the source), are considerable solutions.
- If the transversal intensity profile of the beam that arrives to the crystal is not cylindrically symmetric (even if it is a Gaussian), the waist will not be homogeneous along the ring. Since this pattern does not rotate with the polarization plane, it breaks the main axis symmetry.

- If in the calibration process we use a waveplate, to generate CP, that is not exactly designed for the input wavelength, then it will be elliptically polarized instead of circularly. Then, the calibration alignment can be done wrong, leaving un-homogeneous waists for the ring.
- If there are imperfections in the optical elements or there are dust particles, strange diffraction patterns may emerge, that will make the crests of the conical refraction ring be wavy.
- The crystal or the protective glass of the camera's eye may have double reflections in their walls, that can generate several dimmer rings inside the main one.

Even if a careful calibration should avoid these noises, with the budget limitation of a low-cost device, we find it hard to avoid the fluctuations on the crests of the rings, as well as the non-homogeneity of the waist of the ring. These are clearly appreciable in Figure 16. Thus, these two, together with the pixel-wise Poisson noise are the factors we try to model with the artificial noise in (B.2).

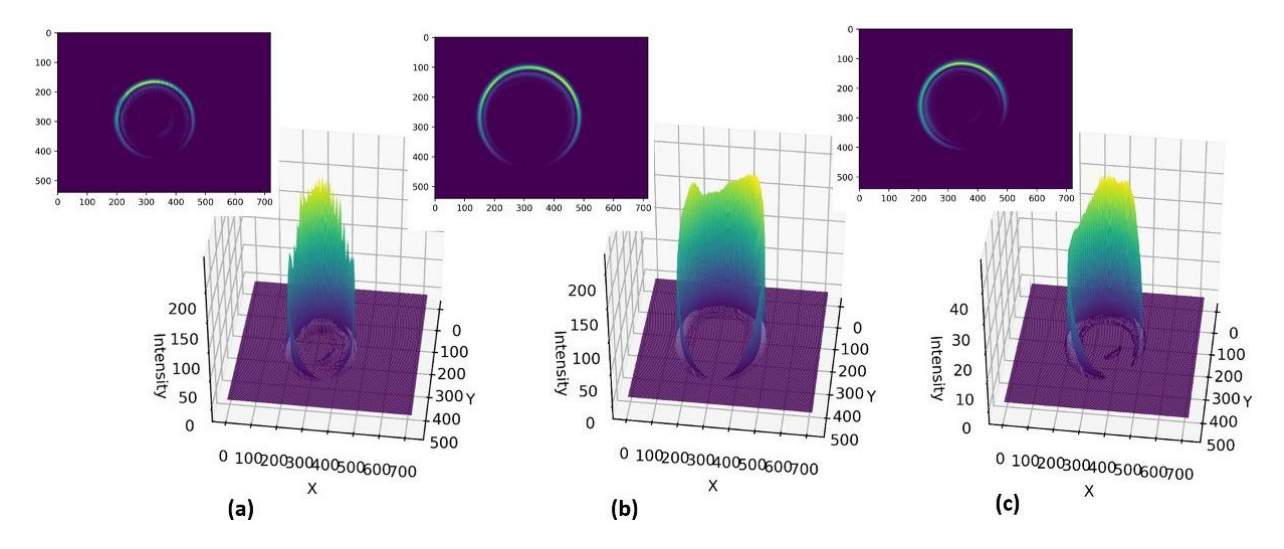


**Figure 16:** Example experimental images as colormaps and surface plots. (a) Image of the He-Ne dataset. (b) Image taken in the LED source setup. (c) Image of the LED dataset.

# C.3. The Experimental Image Dataset

In order to benchmark the designed algorithms (of part B), it is important to have CR crescent ring image pairs labeled with their ground-truth  $\Delta\Phi_{LP}$ . An option for this is to employ another polarimeter with a higher resolution and precision than the one we intend to build. This would allow us to generate a big labeled dataset. Since we had no other polarimeter, this was not an option.

What we could obtain was a certified sample (by DigiPol Technologies) with two crystals that each rotate the linear polarization plane a certified number of degrees (with a precision of  $\pm 0.01$  deg), labeled both for a wavelength of 633 nm and 589 nm (this is in part the reason why we employed the two set-up light sources). With this, for each of the input light beams, we can generate four different crescent CR rings with a known pair-wise  $\Delta\Phi_{LP}$ : a total of 6 different reference-problem pairs. Then, for each set-up we got an additional pair: using two linear polarizers, we can rotate them relatively until they extinguish the output light. At that point the polarizers have their axes orthogonal to each other, meaning they only leave light through at a relative polarization of  $\Delta\Phi_{LP} = \pi/2$  rad.

With all, we built two labeled experimental image datasets of 7 sample-pairs, that can be employed for the final test of the algorithms. Examples of these images can be found in Figure 16.

#### C.3.1. Results of the Algorithms on the Experimental Datasets

Running the same pipeline of (B.10) on the experimental datasets, we get the results that can be found in the /RESULTS folder of the repository [23].

**Table 3:** Sumary of the best variant found for each algorithm on the HeNe laser dataset. Confidence intervals are not shown, since with only 7 samples, they are not significant enough. Std stands for standard deviation.

	Abs. Error (rad)		Times (s)		
Name	Winner Variant	Winner Variant   Mean Std.		Mean	Std.
Cosine squared fit	Opt. Nelder-Mead, final estimation using RANSAC+cos fit	0.50(5) 0.29		2.88	0.012
Blaquez	Opt. Nelder-Mead, final estimation using RANSAC+cos fit	0.51(7) 0.43		0.52	0.020
Blazquez+Cosine Fit	w=0.999, Opt. Nelder-Mead	0.52(4) 0.32		3.43	0.041
Polar Registration	Preproc. Sigmoid k=35, c=0.3	eproc. Sigmoid k=35, c=0.3 0.54		0.26	0.011
Mirror flip	Opt. Quad., Bicubic Interpol., Preproc. Sigmoid k=35, c=0.3	· /		0.14	0.0080
Kalkandjiev-Rotation	Opt. Fibo., Bicubic Interpol., Preproc. Sigmoid k=35, c=0.3			0.22	0.020
Simulation Fit	About Gravic., Opt. Nelder-Mead, Preproc. Norm. to Max	0.58 0.39		1.57	0.042
Relative Rotation	Opt. Quad., Bicubic Interpol., Preproc. Sigmoid k=35, c=0.3	0.61	0.45	0.069	0.0080
Simulation Fit + Embedder	Opt. Quad., Bicubic Interpol., Preproc. Sigmoid k=35, c=0.3	0.88	0.52	2.17	0.033
Bimodal Histogram	Preproc. Sigmoid k=35, c=0.5	1.48	1.59	0.14	0.0025
Gravicenter Regression	Preproc. Sigmoid k=35, c=0.3	2.20	1.96	0.48	0.017
KNN+Embedder	UMAP Embedder, Trained on Non-Noisy Data	2.76	2.05	3.33	0.0
KNN	Trained w. (simulated) Noisy Data	4.23	2.64	1.80	0.0

In Table 3, we gather the best algorithm configurations found for the HeNe light source dataset. As it can be seen, the results are significantly better than those we found for the noisy simulated images. Interestingly, we see that for this intermediate noise level, we find an alternative oredering of the algorithms. It is important to note however, that since the ground-truths are only precise to the second decimal place, in reality the three first algorithms in the table perform equally well in terms of mean absolute error. Having this in mind, the best alternative, even though it has the highest standard deviation, seems to be the Blazquez algorithm, since its computation time is six times smaller than the other two. Note that the ordering in reality is not that surprising, because these first three are closely followed by the Kalkandjiev, Mirror and Simulation Fit algorithms. This means the trend follows an intermediate rationale to the results in the highly noisy and ideal simulated datasets as seen in (B.10.1). The rest of conclusions are akin to the ones in the analysis of (B.10.1).

For the LED dataset (see the repository), we find that the best algorithm is also the Blazquez algorithm, with a mean absolute error of 0.53 deg and a standard deviation of 0.26 (closely followed by the Kalkandjiev and Mirror algorithms).

Considering these results and those in (B.10.1), we can conclude that since depending on the noise level present in the images, the best algorithm turns out to a different one, a full benchmark should be run to know the optimal strategy for any new set-up. This proves the convenience of having developed an extensive algorithm pool, based on different features of the images.

# C.4. The Polarimeter, a Proof of Concept

We can naturally suggest following the discussion of (A.4), the experimental setting of (C.1) and all the algorithms of (B), a device that measures changes in the linear polarization of light. Such a device could have two different configurations: rather the input to the device is the light beam itself,

or the device already has a light source and the input is a sample changing its polarization. The first option would be the convenient one for instance for the detection of exoplanets using LP light [19, 20]. The second one would be the convenient one for the pharmaceutical enantiomerism or optical concentration measurements of the food/berverage industry, as commented in (A.4). In fact, this second configuration is the one found most typically in a laboratory, which if it only requires the user to input the sample and wait for the results, is commercially knwon as an **automatic polarimeter**. Because in this option, the light beam and its parameters, which affect so critically to the conical refraction phenomenon, are under our control, we decided opted for such a configuration, following the prototype built in Ref. [13] by Lizana et al.

By now it is clear that device will have three parts of different nature: an *optical part* with the components described in (C.1); an *electronic part* encompassing both the camera and the computer to convert the images into meaningful information; and, the main merit of the present thesis: the *algorithmic part*, that will rule the measurement of the polarization and will interact with the user. With this scheme, let us present a proof-of-concept of the device (see Figure 17):

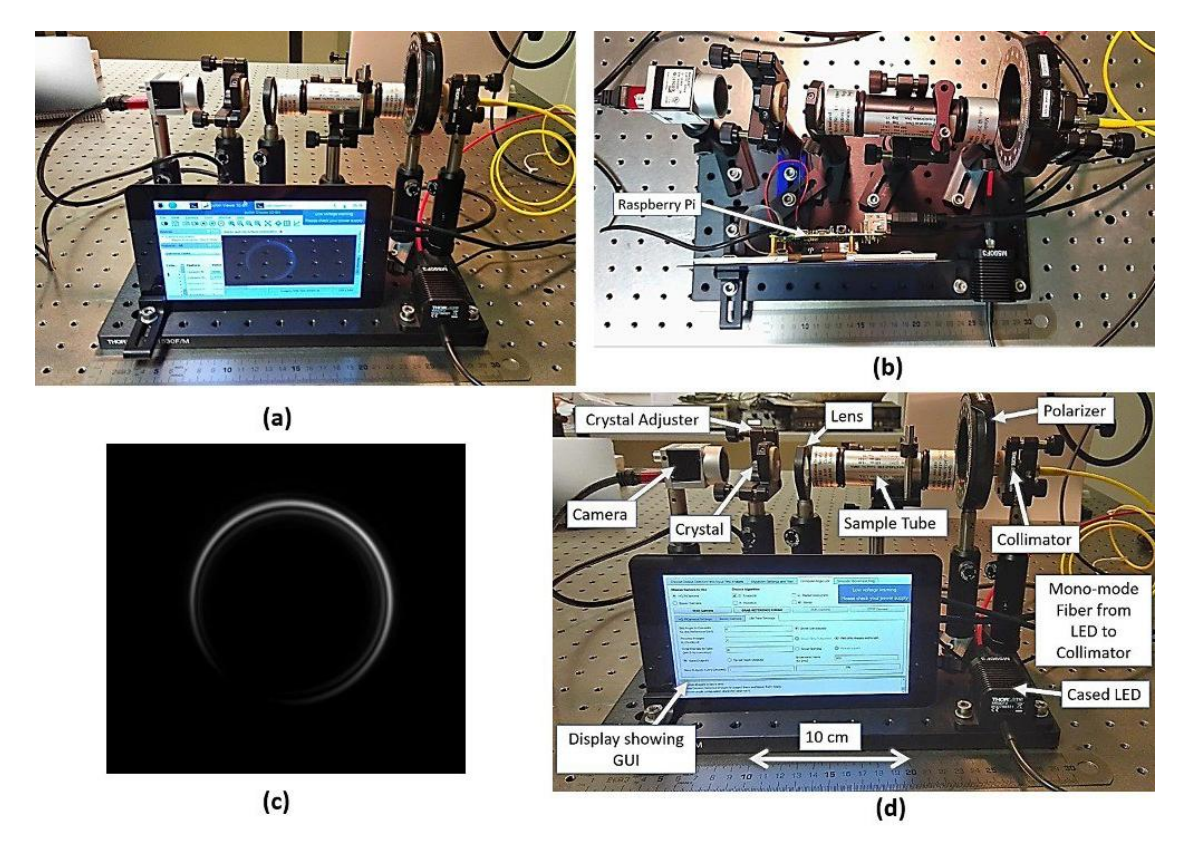


Figure 17: The proof-of-concept polarimeter. (a) Frontal view. (b) Superior view. (c) Image taken by its camera and part of the proof-of-concept dataset. (d) Details of the components of the prototype.

- Optical Part: A LED M590F3 590 nm 3.3 mW light source, coupled to a single-mode fiber and a collimator, consuming 3V at 950mV. A convergent lens with 100 mm focal length. A monoclinic centrosymmetric  $KGd(WO_4)_2$  rectangular biaxial crystal of sizes  $6 \times 4 \times 20mm$ .
- Electronic Part: A Basler acA720-520um camera. A Raspberry Pi 4 mini-computer with 4Gb of RAM. A Raspberry Pi 3 7" Touchscreen Display for user interaction with the computer.
- Algorithmic Part: A graphical user interface (GUI) application, programmed using Python and the PyQt library [57], with all the algorithms of part B available within it, allowing the user to fully customize their parameters. The dependencies and a small manual, together with all the code can be found in the repository [23]. Essentially, it allows: (a) the determination of  $\Delta\Phi_{LP}$  for two particular takes; (b) a continuous real-time monitoring of  $\Delta\Phi_{LP}$  (relative to an initial reference LP); (c) the simulation of theoretical images. The touchscreen in Figure 17.d is showing the GUI.

Note that we have placed no magnification of the ring prior to the camera, which means the images that will be captured will have a lower resolution than those with which we worked in the rest of the work (the image in Figure 17.c has  $170 \times 160$  pixels, against the  $540 \times 720$  of the ones in Figure 16). In part this was because in the basis of the device there was not enough space for that. Yet this is not the only reason, for it could be solved by placing a mirror in the corner where the camera is, and placing the camera in the next corner, to allow the addition of a second lens (requiring a lengthen optical path). The main reason was that we decided to stick to a simpler configuration to make the device robuster to noise and to de-calibration. Even if the resolution is smaller, using a lens less introduces much less noise in the images and the device is simpler to be calibrated and harder to be de-calibrated by accidental hits. Moreover, if the final version is to include the Pi camera with a higher pixel density, as we explain in the next section, the magnification will not be needed at all.

#### C.4.1. Proof-of-concept Dataset and Algorithm Check

We generate a small labeled dataset following the same steps as for (C.2), now employing the proof-of-concept. We use it for testing the algorothms using the pipeline explained in (B.10.). The full results can be found in [23], but the main highlights are the following ones:

- The best algorithm for the proof-of-work turns out to be the Simulation Fit algorithm, using the geometric center fix, preprocessing the images to the mean value and using the Nelder-Mead optimizer. It gives a mean absolute error of 0.72 deg with a standard deviation of 0.45 deg. The average time taken per image is of 0.36 s.
- It is followed by the Kalkandjiev-Rotation algorithm (B.6.3.) with the Quadratic Fit search algorithm and using cubic interpolation. It gives an average absolute error of 0.81 deg and a standard deviation of 0.74 deg. The average time taken per image is of 0.07s.

These resulting precisions are comparable to those obtained with the full magnified ring set-up in (C.2), so we can consider the hand-made low-cost prototype to be a success.

#### C.4.2. Cost Analysis

We can estimate an upper bound of the production cost of the device by the cost of its components in the general customer market. See a summary in Table 4. Note that if the device was mass produced the price of the components would drop significantly. Also, notice that we assume that all the casing and support materials could be made using a 3D printer, with all the optical elements readily aligned and an adjustable part to calibrate the crystal's orientation. This casing would protect and fix all the components, only leaving an opening to introduce the sample and the access to the touchscreen.

Component	Vendor	Price (euro)	
Polarizer film	Thorlabs	9	
3V 1A Power Supply for light source	Amazon	10	
Lens 100 mm	Thorlabs	19	
Casing and element support 3D printer material	Estimated	50	
Raspberry Pi 4	Amazon	40	
Raspberry Touchscreen 7"	Farnell	50	
Single-mode fiber apt for 590 nm	Thorlabs	72	
Biaxial crystal cut in the right crystalographic plane	Altechna (priv. comm.)	300	
LED M590F3 - 590 nm $3.3 \text{ mW}$	Thorlabs	430	
Basler acA720-520um camera	Basler	330	
Total	-	1310	

Table 4: Table with the general customer rounded prices of the components of the proof-of-concept.

Very importantly, note that we do not require all the features offered by the Basler camera (like the 525 frame per second rate), such that for example the High Quality Pi Camera of Raspberry would be

enough. This second camera is sold for 50 euro (Farnell) and has actually a bigger resolution (12.3 MP) than the Basler camera, meaning higher precision measurements would be obtained. This is not only for the increase in the number of pixels, but is especially due to the fact that its pixels have a smaller pitch of 1.55  $\mu m$  (compared to the 6.9  $\mu m$  sized Basler pixels), which means that possibly without magnification the same effective resolution as the test images of set-up (C.1) could be obtained.

Let us leave the component price at 1010 euros (for the substitution of the Basler camera by the Pi camera). Then, once the case is printed, by considering that mounting the device, callibrating it and installing the necessary dependencies and software, takes about 2 hours, if we assume a 30 euro/h handwork: we could get a fully operational automatic polarimeter based on the proof-of-concept by 1070 euros. This would then be the upper bound of its production cost.

#### C.4.3. A Comparison with Commercial Automatic Polarimeters

### Qualiltative Comparison

Commercial automatic polarimeters work in a very different way to ours [58]. They have a mechanically movable linear polarizer and an intensity measuring device after-wards. The polarizer is rotated from a fixed initial position until a maximum intensity angle is found (or the no intensity angle, which by orthogonality also indicates the direction of polarization). Then, for the next sample, the linear polarizer goes back to its initial position and a new measurement is taken. The relative angle  $\Delta\Phi_{LP}$ is given by the difference in the rotation of the polarizer. The precise measurement of this rotation is typically done using chains of gears (or similar components) that can rotate the linear polarizer by a fixed angular amount. Essentially, this amount gives the precision of the polarimeter. Clearly it is a very robust technique for its simplicity, but it has its own drawbacks. On the one hand, the mechanical setting makes the device have a considerable weight and dimensions. Most importantly however, the need to move a mechanical setting and to take measurements in each small displacement makes the device require as much as a few seconds for the maximum precision in each measurement (we will see that even the fastest polarimeters require at least 1 second). This means a real time monitoring only offers a maximum of a single measurement per second, which might be pointless for kinetic constant determination in fast chemical reactions. In addition, the precision of the measurements is bounded by how small the displacements are feasible to be made mechanically, given they should be done in a reasonable time and the device should occupy a reasonable space.

In contrast, our device is a "snapshot" polarimeter, which only requires to take a photo and process it to obtain all the information about the polarization. This is because the CR phenomenon naturally acts as a continuous set of linear polarizers in all possible orientations. At a single time, it gives us the amount of light that each possible linear polarizer would allow to pass in each angular position. The limitation of course, is that the digitalization must be done with a discrete pixel array. Yet it is true that, this transferral of the mechanical problem into a digital one not only means the importance is now placed in the algorithms to resolve the computer vision task, but especially means the resolution with which we can discern a variation of the angle, is not limited by the physics of the gears, but by the resolution density of the camera taking the image (which unfortunately is quite poor for our camera). In contrast with the finer gear development, it is well known that the camera industry is developed independently of the polarimetry industry, meaning the precision of the device would benefit "for free" from the progress made by such a powerful sector.

#### Quantitative Comparison

In Table 5, we have gathered some commercially available automatic polarimeters. As it can be seen, these polarimeters offer a better precision than our proof-of-concept. Yet, none of the precisions is better than our achievable precision (as seen in the tests in B.10.); which could in principle be attained by increasing the resolution of the taken ring images, by reducing the noise with better quality optical components or a more precise alignment using a 3D printed mould, and by calibrating the crystal's orientation with electronic control.

Polarimeter Brand and model	Price (euro)	Accuracy (deg)	Source	Features
Krüss Polarimeter P3000 Cat. N. 10 61 13000	8,150 + VAT	±0.01	LED 589 nm	- Fast Meas. time $\sim 1s$ - Thermometer - 28 kg; 645 x 200 x 360 mm
Krüss Polarimeter P8000 Cat. N. 63 61 80000	12,247 + VAT	±0.003	LED 589 nm	- Fast Meas. time $\sim 1s$ - Thermometer - 28 kg; 645 x 200 x 360 mm
Krüss Polarimeter P8100-TF Cat. N. 10 61 18104	22,544 + VAT	±0.002	LED 589 nm	- Fast Meas. time $\sim 1s$ - Thermometer - Sample temperature control - Flow through and drying unit - 28 kg; 645 x 200 x 360 mm
Schmidt&Haensch Polartronic V 201 SC	18,360 + VAT	±0.005	LED	- Two fixed wavel. to choose in $\{405, 435, 546, 578, 589, 633, 882\}$ - Thermometer - Meas. time $\sim 4s$ - $18.3$ kg; $730 \times 370 \times 160$ mm

Table 5: Some commercial automatic polarimeters sold in 2022 by IRMECO, a German laboratory supplier.

Following the previous qualitative observations, we can note several points in comparison with our device, to layout the potential niches it could cover:

- The measurement times are in all cases slower than in our device. In fact, all these Krüss polarimeters belong to a same assortments of automatic polarimeters, which according to their manual [60], from 2003, when they patented the fast measurement protocol (until at least 2016, the date of the manual), "are the fastest" automatic "polarimeters in the world". And they are an order of magnitude slower than ours (in its preliminary version). Then, a potential target for our polarimeter could be the sector needing fast real-time polarization measurements. These presumably include the chemistry community employing polarization measurements for non-invasive concentration monitoring to get the kinetic constants of chemical reactions.
- They are all considerable in size and weight, as opposed to our device. In its current version our device weights about 2 kg (which can be made lighter using the 3D printed casing and holders) and measures 150 x 200 x 300 mm, which can be reduced a half in the vertical axis of 200 mm, by setting the optical components in the same height as the display. Moreover, since as power input, we only require to feed the LED and the Raspberry Pi, a portable rechargable battery could be installed. This means our device could potentially also target the customers that prefer a portable and lightweight version of the device. Such an example could be University teaching laboratories or field researchers.
- They all include a thermometer and some include sample temperature control devices or tubes and extra components to allow live flow of samples through the device instead of using a static tray. The thermometer is not an expensive component, so it could easily be implemented in our device. When it comes to the rest of components, we see that they include them at the cost of about 10,000 euro (comparing the second and third model of the table, which are the same otherwise). With this difference, we could presumably include them as well.
- Finally, the prices of the polarimeters are significantly bigger than the production cost of our device, even in its home-made version. Since any customer prefers a cheaper device, this is a hook for any potential client.

With all, even if there are many points which must be improved for a fully functional and competitive prototype, our device seems to allow many possible specializations to fit the different niches we described.

# Conclusions and Future Work

In a nutshell, using the theoretical properties of CR, we have developed a considerable collection of algorithms to predict the linear polarization of light given a CR crescent ring image. We have tested them against theoretical simulated images with and without noise, and against experimental labeled images. We have obtained an experimental precision of  $\pm 0.5$  deg, with an ideal obtainable precision of  $\pm 0.001$  deg using the same camera resolution. Both of them shall improve significantly with the use of a camera with smaller pixels (thus, higher resolution for the same rings). We have then crafted a low-cost proof-of-concept automatic polarimeter and tested the algorithms on it, to obtain a precision of  $\pm 0.7$  deg. The difference was mainly due to the fact that we omited the magnification step to reduce lens noise and to give robustness to the device. Both of these results are nevertheless already better than the previously reported CR polarimeter in Ref. [13], where a precision of 2.6 deg was obtained. We have also analyzed the market of automatic polarimeters and have seen that our device has a big potential to compete with top sold (and expensive) polarimeters. We have proposed several directions into which we could continue building prototypes, from a more expensive one trying to refine the procedure to the maximum, to an even cheaper, more versatile and portable one, which would at least have the precision of our handmade prototype.

Aside exploring all the ideas towards the improvement of the proof-of-concept, it is left as a future work to test which is the limit in the obtainable precision by only increasing the pixel density of the camera. If the rest of optical setting is refined into industrial accuracy (avoiding a handmade process as ours), this could mean the device has the potential to be the most precise of the automatic polarimeters. This is a serious consideration because the phenomenon, in theory, offers an infinite degree of precision in a single image, only spoiled by the experimental noise and the necessary discretization of a camerasensor. When it comes to the algorithms, the deep learning approach to the problem still needs to be thoroughly explored. Also, it is left as future work to test whether the extension of the Blazquez algorithm suggested in section (B.6.7) could really lead us to a groundbreaking algorithm.

All in all, if there is a message to be learned from this work, it is that although it was tabled almost 200 years ago, the beautiful proof of the mighty power of mathematics by Fresnel and Hamilton, known today as conical refraction, has still an endless potential to be unchained.

### Acknowledgments

I would like to thank Alex Trupin for all those hours in the lab calibrating Concical Refraction rings, for all his advice and invaluable help. Thanks for all the patience you have had with my clumsiness in experimentation, for answering all my questions and requests for finner and finner rings. Thanks for explaining me once and again the essentials and tricks of an optics laboratory. You have gave me an invaluable knowledge. *Per aquesta aventura i per totes les que vinquin!* 

Thanks a lot to Jordi Mompart, who was the one who opened me the door (once again) to such an interesting project. Thanks for all the trust you place on me in every adventure we share! Jamás podré agradecerte lo suficiente. Hope the work is up to your expectations!

Thanks to Carles Blazquez for his inestimable contribution to the algorithms. It turns out your algorithm is one of the robustest! ¡Quizá algún día descubras el color del cielo de uno de los exoplanetas que estudias con tu propio algoritmo! ¡Espero estar ahí cuando suceda!

And of course, my deepest gratitude to Todor Kirilov Kalkandjiev. An exemplary scientist and professor, and an even greater person, who I admire and is for me a reference who showed me that it is possible to live with this love towards the *thaumazein*, the fascination in front of this world, until the last one of our days. I wish you could see the results of your project and we could continue together the path towards the device you had in mind. This work is because of you, and is entirely for you.

Si, al final me debes una caña;)

# References

[1] The complete version of the thesis can be found in the Github repository of the project. In the following link in its edition to be printed:

https://github.com/Oiangu9/Conical\_Refraction\_Polarimeter/blob/main/THESIS\_PRINT\_ed\_Conical\_Refraction\_Polarimeter.pdf

And in the following link in its edition for online reading:

https://github.com/Oiangu9/Conical\_Refraction\_Polarimeter/blob/main/THESIS\_READ\_ed\_Conical\_Refraction\_Polarimeter.pdf

- [2] L. D. Landau and E. M. Liftschift. Electrodynamics of Continuus media. 2nd Edition. (Oxford, 1960)
- [3] D. D. Stancil. Theory of Magnetostatic Waves. Springer New York (1993).
- [4] B. E. A. Saleh and M. C. Teich. Fundamentals of Photonics. New York Wiley. (1991)
- [5] A. M. Belskii and A. P. Khapalyuk. Internal conical refraction of bounded light beams in biaxial crystals. Opt. Spectrosc. 44, 436 (1978).
- [6] A. M. Belskii and A. P. Khapalyuk. Propagation pf confined light beams along the beam axes (axes of single ray velocity) of biaxial crystals. Opt. Spectrosc. 44, 312 (1978).
- [7] M. V. Berry . Conical diffraction asymptotics: fine structure of poggendorff rings and axial spike. J. Opt. A: Pure and App. Opt. 6, 289 (2004)
- [8] M. V. Berry and M. R. Jeffrey. Chapter 2 Conical diffraction: Hamilton's diabolical point at the heart of crystal optics. Progress in Optics. Elsevier. Volume 50, (2007), Pages 13-50
- [9] M. R. Jeffrey. Conical Diffraction: Complexifying Hamilton's Diabolical Legacy. Doctoral thesis (2007).
- [10] A. Turpin. Conical Refraction: Fundamentals and Applications. Doctoral Thesis (2015).
- [11] T. K. Kalkandjiev and M. A. Bursukova. *Conical refraction: an experimental introduction*. Proc. SPIE 6994, Photon Management III, 69940B (2008)
- [12] Turpin, Alex, et al. "Conical refraction: fundamentals and applications." Laser & Photonics Reviews 10.5 (2016): 750-771.
- [13] Lizana, A., et al. "Implementation and performance of an in-line incomplete Stokes polarimeter based on a single biaxial crystal." Applied Optics 54.29 (2015): 8758-8765.
- [14] Peinado, Alba, et al. "Optimization, tolerance analysis and implementation of a Stokes polarimeter based on the conical refraction phenomenon." Optics express 23.5 (2015): 5636-5652.
- [15] Peinado, Alba, et al. "Snapshot polarimeter based on the conical refraction phenomenon." Modeling Aspects in Optical Metrology V. Vol. 9526. SPIE, (2015).
- [16] F. A. Carey & R. J. Sundberg. Advanced Organic Chemistry. Part A: Structure and Mechanisms. Springer New York, NY. (2007).
- [17] B. D. Cameron et al. Noninvasive glucose sensing utilizing a digital closed loop polarimetric approach. IEEE Trans. Biomed. Eng. 44, 1221-1227 (1997).
- [18] L. A. Vitking et al. Polarization studies in multiply scattering chiral media. Opt. Eng. 39, 353-362 (2000).
- [19] Berdyugina, Svetlana V., et al. "First detection of polarized scattered light from an exoplanetary atmosphere." The Astrophysical Journal 673.1 (2007): L83.
- [20] D. Gisler et al. CHEOPS/ZIMPOL: a VLT instrument study for the polarimetric search of scattered light from extrasolar planets Proc. SPIE 5492, 463-474 (2004).
- [21] J. S. Tyo et al. Review of the passive imaging polarimetry for remote sensing applications. Appl. Opt. 45, 5453-5469 (2006).

- [22] J. C. Ramella-Roman et al. *Polarized light imaging with a handheld camera*. Proc. SPIE 5068, 284-293 (2003).
- [23] Github repository of the present thesis, with all the implemented software, the GUI app and numerical results can be found at:
  - https://github.com/Oiangu9/Conical\_Refraction\_Polarimeter
- [24] C. R. Harris et al. Array programming with NumPy. Nature 585, 357–362 (2020).
- [25] J. Bradbury et al. JAX: composable transformations of Python+NumPy programs. (2018)
- [26] A. Collette.  $Python\ and\ HDF5.$  (2013) Open source Python library h5py. Main page: https://www.h5py.org/. Documentation: https://docs.h5py.org/en/stable/
- [27] P. Soille Morphological Image Analysis: Principles and Applications. Springer Science & Business Media, 2013
- [28] R. P. Brent. Algorithms for minimization without derivatives. Prentice-Hall, 1972
- [29] D. E. Ferguson. Fibonaccian searching. Communications of the ACM. 3 (12): 648. (1960)
- [30] J. A. Nelder, R. Mead. A simplex method for function minimization. Computer Journal. 7 (4): 308–313. (1965)
- [31] M. J. D. Powell. An efficient method for finding the minimum of a function of several variables without calculating derivatives. Computer Journal. 7 (2): 155–162. (1964)
- [32] T. Head et al. scikit-optimize/scikit-optimize (v0.8.1). Zenodo (2020). Main page: https://scikit-optimize.github.io/stable/index.html
- [33] Bradski, G. *The OpenCV Library*. (2000). Employed in its Python library version *cv2*. Main page: https://opencv.org/ Documentation page: https://docs.opencv.org/4.x/index.html
- [34] K. Turkowski, (1990). Filters for Common Resampling Tasks. In Glassner, Andrew S. (ed.). Graphics Gems I. Academic Press. pp. 147–165.
- [35] F. Pedregosa et al. *Scikit-learn: Machine Learning in Python*, JMLR 12, pp. 2825-2830, 2011. Main page of library: https://scikit-learn.org/stable/index.html.
- [36] S. Van der Walt et al. scikit-image: image processing in Python. Peer J. 2, p.e453. 2014
- [37] E. De Castro and C. Morandi Registration of Translated and Rotated Images Using Finite Fourier Transforms, IEEE Transactions on Pattern Analysis and Machine Intelligence, Sept. 1987
- [38] B. S Reddy and B. N. Chatterji, An FFT-based technique for translation, rotation, and scale-invariant image registration, IEEE Transactions on Image Processing 5, no. 8 (1996): 1266–1271.
- [39] N. Otsu. A threshold selection method from gray-level histograms. IEEE Trans. Sys. Man. Cyber. 9 (1): 62–66. (1979)
- [40] Bretscher, Otto (1995). Linear Algebra With Applications (3rd ed.). Upper Saddle River, NJ: Prentice Hall.
- [41] M. A. Fischler and R. C. Bolles. Random Sample Consensus: A Paradigm for Model Fitting with Applications to Image Analysis and Automated Cartography. Comm. of the ACM 24 (6): 381-395. (1981)
- [42] A. Paszke et al. PyTorch: An Imperative Style, High-Performance Deep Learning Library. In Advances in Neural Information Processing Systems 32. Curran Associates, Inc., pp. 8024–8035. (2019)
- [43] M. A. Nielsen. Neural Networks and Deep Learning. Determination Press, 2015.
- [44] D. P. Kingma et al. Adam: A method for stochastic optimization. arXiv:1412.6980 (2014).
- [45] Manifold Learning. Article in scikit-learn's documentation: https://scikit-learn.org/stable/modules/manifold.html

- [46] J. L. Bentley. Multidimensional binary search trees used for associative searching. Communications of the ACM (1975)
- [47] I. Borg and P. Groenen. Modern Multidimensional Scaling Theory and Applications Springer Series in Statistics (1997)
- [48] J.B. Tenenbaum et al. A global geometric framework for nonlinear dimensionality reduction. Science 290 (5500)
- [49] L. McInnes et al. *UMAP: Uniform Manifold Approximation and Projection*. The Journal of Open Source Software, 3(29), 861. 2018.
- [50] L. McInnes et al. UMAP: Uniform Manifold Approximation and Projection for Dimension Reduction. arXiv preprint arXiv:1802.03426 (2018).
- [51] J. Goldberger et al. *Neighbourhood Components Analysis*, Advances in Neural Information Processing Systems, Vol. 17, May 2005, pp. 513-520.
- [52] S. Roweis & L. Saul, Nonlinear dimensionality reduction by locally linear embedding Science 290:2323 (2000)
- [53] Roughgarden T. and G. Valiant, CS168: The Modern Algorithmic Toolbox Lecture #9: The Singular Value Decomposition (SVD) and Low-Rank Matrix Approximations. Lecture Notes. (2015)
- [54] B. Schölkopf, Bernhard; et al. Nonlinear Component Analysis as a Kernel Eigenvalue Problem. Neural Computation. 10 (5): 1299–1319 (1998).
- [55] A. Hermans et al. In defense of the triplet loss for person re-identification. arXiv preprint arXiv:1703.07737 (2017).
- [56] N. E. Helwig. Nonparametric Bootstrap in R. Notes. University of Minnesota. (2021)
- [57] M. Summerfield. Rapid GUI Programming with Python and Qt: the Definitive Guide to PyQt Programming. Upper Saddle River, NJ: Prentice Hall, 2008.
- [58] R. Paschotta. RP Photonics Encyclopedia.
- [59] E. T. Jaynes. Probability Theory as Logic. Maximum-Entropy and Bayesian Methods. Kluwer, Dordrecht, 1990.
- [60] Manual for the Krüss automatic polarimeters found in their official page: kruess.com https://www.kruess.com/wp-content/uploads/2021/02/BR\_Polarimeter\_en\_3.2.pdf